DEVELOPING EPITAXIAL GRAPHENE ELECTRODES FOR SILICON CARBIDE BASED OPTOELECTRONIC DEVICES

A Thesis Submitted to
The Graduate School of Engineering and Sciences of
İzmir Institute of Technology
In Partial Fulfilment of the Requirements for the Degree of

MASTER OF SCIENCE

in Material Science and Engineering

By
Erdi KUŞDEMİR

December 2015
İZMİR

We approve the thesis of **Erdi KUŞDEMİR**

Examining Committee Members:

_____

Assist. Prof. Dr. Cem ÇELEBİ
Department of Physics, İzmir Institute of Technology

_____

Assist. Prof. Dr. Cumhur Gökhan ÜNLÜ
Department of Biomedical Engineering, Pamukkale University

_____

Assoc. Prof. Dr. Serkan ATEŞ
Department of Physics, İzmir Institute of Technology

28 December 2015

_____

Assist. Prof. Dr. Cem ÇELEBİ
Supervisor, Department of Physics,
İzmir Institute of Technology

_____

Assoc. Prof. Dr. Hâldun SEVİNÇLİ
Co-Adviser, Department of Material
Science and Engineering,
İzmir Institute of Technology

_____

Prof. Dr. Mustafa M. DEMİR
Head of the Department of
Material Science and Engineering

_____

Prof. Dr. Bilge KARAÇALI
Dean of the Graduate School of
Engineering and Sciences

ACKNOWLEDGEMENTS

I would like to express my gratitude to my advisor Assist. Prof. Dr. Cem Çelebi for his invaluable advice, guidance and encouragement throughout this study.

I also would like to thank my friends Dilce Özkendir, Damla Yeşilpınar, Sırrı Batuhan Kalkan, Alnazir İbrahim, Halis Güzelaydın, Gündoğdu Şahin and Elif Bilgilisoy for their encouragement, help and patience all along.

I am thankful to Onur Serbest from Sabanci University Nanotechnology Research and Application Center (SUNUM) for his support and help during device fabrication processes. I would like to acknowledge the financial support from Scientific and Technological Research Council of Turkey (TÜBİTAK) for this thesis.

And last but not least, I am also grateful to my family for leading me to this stage and for their endless support during all of my life.

ABSTRACT

DEVELOPING EPITAXIAL GRAPHENE ELECTRODES FOR SILICON CARBIDE BASED OPTOELECTRONIC DEVICES

In this thesis work, I studied the fabrication and characterization of graphene-semiconductor-graphene ultraviolet photodetector based on the rectifying character of Schottky junction at the interface between epitaxial graphene and silicon carbide semiconductor. As-grown single layer epitaxial graphene is interdigitated as transparent conductive electrode to probe photo-generated charge carriers in a semi-insulating 4H-silicon carbide substrate. The fabricated device exhibits the typical current-voltage characteristics of a conventional metal-semiconductor-metal type photodetector with low leakage current. Time-resolved photocurrent measurements suggest an excellent photocurrent reversibility and high response speed of the device. The measurements performed for different illumination wavelengths showed that the sample reveals higher responsivity values when it is exposed to the light with 254 nm wavelength. The obtained results imply that epitaxial graphene can be used readily as transparent conductive electrode for SiC based optoelectronic device applications.

Finally, in the last chapter, I discuss how the photoresponsivity of the graphene-semiconductor-graphene photodetector can be enhanced by CdTe/CdS quantum dots. The drop casted CdTe/CdS quantum dots have been shown to increase the photoconductivity of the device. The thickness of the quantum dots is found to effect the enhancement factor of the photoresponsivity of the device.

ÖZET

SİLİSYUM KARBÜR TABANLI OPTOELEKTRONİK CİHAZLAR İÇİN EPİTAKSİYEL GRAFEN ELEKTROTLAR GELİŞTİRİLMESİ

Bu çalışmada grafen-yarıiletken-grafen tabanlı ultraviyole bölgesinde çalışan foto-detektörün fabrikasyon ve karakterizasyonunu gerçekleştirdim. Bu aygıt yapısının temel özelliği gösterdiği Schottky ekleminin düzenleyici etkisidir. Hiçbir dış etkiye ihtiyaç duymaksızın büyütülebilen epitaksiyel grafen, yarı-yalıtkan haldeki 4H-SiC alt taşın üzerine, optik olarak geçirgen ve elektronik olarak iletken elektrot amacı ile işlenmiştir. İşlenen bu elektrotlar ile 4H-SiC içinde fotonların etkisi ile üretilen yük taşıyıcılarının ölçümlenmesi hedeflenmiştir. Yapılan akım-voltaj ölçümleri sonucunda üretilen cihaz geleneksel metal-yarıiletken-metal yapısındaki foto-detektörlerinde gösterdiği gibi düşük kaçak akım değerleri göstermiştir. Yapılan zamana bağımlı foto-akım ölçümlerinin sonucunda aygıtın yüksek hızlı tepkiler verdiği ve verdiği tepkilerin kendini mükemmel bir şekilde yenileyebildiği gözlemlenmiştir. Tüm ölçümler farklı dalga boylarındaki ışık kaynakları ile tekrarlansa da aygıt 254 nm dalga boyuna en yüksek tepkiyi vermiştir. Elde edilen sonuçlar açıkça göstermektedir ki; grafen şeffaf bir elektrot olarak, SiC tabanlı foto-detektör uygulamalarında rahatlıkla kullanılabilir.

Üretilen grafen-yarıiletken-grafen aygıtından elde edilen verimliliğin, aygıta eklenen CdTe/CdS tabanlı kuvantum noktaları ile arttırabilmektedir. Basitçe aygıtın üzerine damlatılan kuvantum noktalarını, aygıtın foto-iletkenlik değerlerinde artışa yol açmıştır. Aygıtın foto-iletkenlik değerlerinin eklenen kuvantum noktaları katmanının kalınlığı ile ilintili olarak değiştiği gözlemlenmiştir.

TABLE OF CONTENTS

LIST OF FIGURES

Figure **Page**

LIST OF TABLES

Table **Page**

LIST OF ABBREVIATIONS

Abbreviation	Description
2D	Two-dimensional
AFM	Atomic Force Microscopy
CVD	Chemical Vapor Deposition
DI	Deionized
GSG	Graphene-Semiconductor-Graphene
ITO	Indium Tin Oxide
LED	Light Emitting Diode
MSM	Metal-Semiconductor-Metal
NPDR	Normalized Photo to Dark Current Ratio
OLED	Organic Light Emitting Diode
PCEF	Photocurrent Enhancement Factor
QD	Quantum Dot
RIE	Reactive Ion Etching/Etcher
SBH	Schottky Barrier Height
SI	Semi-Insulating
SiC	Silicon Carbide
UHV	Ultra High Vacuum
UV	Ultra Violet
UV-Vis	Vis Ultraviolet-Visible

CHAPTER 1

INTRODUCTION

1.1. What is Graphene?

Two dimensional sheet of sp^2-hybridized carbon is called graphene. The honeycomb structure of graphene sheet is the basic building block of the other allotropes, such as the 3D stacked form called graphite, 1D rolled form called carbon nanotubes and 0D wrapped form of fullerenes. The graphene sheets have attracted a lot of theoretical and recently experimental studies due to its magnificent thermal, mechanical and electrical properties, arising from the long range π-conjugation.

Experimental studies on graphene started with utilizing fewer and fewer layers of graphite [1], the field was delivered a jolt in 2004, when Geim and co-workers at Manchester University first isolated single-layer samples from graphite. The finding disproved the misconception about the long-assumed instability of 2D crystals at finite temperatures [2]. The supporting substrate, which have significant effects on growth and the electrical properties of the sample, stabilizes the quasi-two-dimensional films in molecular beam epitaxy technique [3]. Yet the graphene sheets acquired by the Manchester group were obtained using the mechanical exfoliation technique, which resulted single and few layer graphene flakes pinned to the substrate by only Van der Waals forces, and could be easily made free-standing by etching away the substrate [4], [5]. Thus the induced effects from the presence of substrate were minimized and the intrinsic properties of graphene could be probed by scientists.

Experimentally isolated single-layer graphene revealed a large amount of undiscovered, interesting physics [6], [7]. Graphene's ambipolar field effect [8], the quantum Hall effect at room temperature [9], [10], measurements of extremely high carrier mobility [11], and even the first ever detection of single molecule adsorption events [12] were the initial studies conducted around the world. The interesting properties revealed by the studies on single-layer graphene suggested the exciting probability of implementation of graphene in a myriad of devices, including sensors, the next generation

high-speed and radio frequency logic devices, transparent electrodes for displays and solar cells, thermally and electrically conductive reinforced composites.

1.2. Graphene as an Electrode Material

The unique properties such as excellent optical transparency, high electrical conductivity and mechanical flexibility make graphene a desirable material as a conductive electrode for next generation photodetectors and solar cells. Conventionally during the decade Ni/Au, Ti, TiW and indium tin oxide (ITO) have been implemented as a transparent electrode to collect photo-generated charge carriers in optoelectronic and photovoltaic devices [13]–[17]. But the very low transmittance (<80%) of these materials especially in the ultraviolet (UV) region below 400 nm arising from high surface reflection and absorption have been an undesired issue for the implementation of transparent electrodes to devices functioning at the UV region. Differing from the forementioned transparent contact materials, graphene is found to be capable of transmitting more than 90% of the light in the wavelength range between 200-400 nm [17], [18]. Combining this high UV transmission level with the zero band gap property makes graphene a promising candidate as a transparent and conductive electrode for such devices. Recently it is shown that a multilayer graphene template grown by chemical vapor deposition (CVD) technique can be utilized as a transparent Schottky electrode for GaN based metal-semiconductor-metal (MSM) type UV sensor [19].

1.3. Production of Graphene

Various different production methods were devised to manufacture large-scale graphene, such as epitaxial growth on silicon carbide [20]–[22] and ruthenium [23], along with two dimensional assembly of reduced graphene oxides [24] and exfoliated graphene sheets [8], CVD of carbon atoms on transition metals [25], following the initial discovery of isolated graphene extracted from graphite crystals by exfoliation method. Multilayer graphene specimens that are tightly bound to their substrates can be obtained utilizing epitaxial growth with superior quality, however electrically isolated mono- or bilayer graphene suitable for device applications has not been realized yet. Despite this downside, low-cost synthesis and production of large-scale graphene transparent films by the self-

assembly of soluble graphene sheets holds promise for the future. Nevertheless; these assembled graphene films are plagued with inferior electrical conductivity stemming from the vigorous exfoliation and reduction processes in the production stages that cause excessive interlayer junction resistance and introduce structural defects into the structure.

1.4. Outline

This thesis covers the graphene-semiconductor-graphene (GSG) UV photodetector we fabricated, where an as-grown single layer epitaxial graphene is implemented as transparent, conductive electrode on a nominally semi-insulating (SI) 4H-SiC substrate. The response of the fabricated GSG device with interdigitated epitaxial graphene electrodes is characterized in the absence and in the presence of a narrow band UV light irradiation with different wavelengths. Our device is found to reveal the typical current-voltage (I-V) characteristics of a conventional MSM photodetector with a low leakage current and high response speed. Same electronical characterization experiments repeated after adding colloidal Quantum dots to the device.

CHAPTER 2

GRAPHENE, PROPERTIES AND RECTIFICATION CHARACTER

2.1. Morphological Structure of Graphene

As brought up in the previous chapter, graphene is a two-dimensional material made of carbon atoms emplaced along a honey-comb lattice. Elemental carbon, which is situated in the Group IV of the periodic table consists of 6 electrons, 4 of which are the valance electrons situated in *2s* and *2p* orbitals. Such kind of electronic configuration allows sp^2 and sp^3 hybridization which are seen in in-plane bonding and diamond crystal structures respectively. Hybridization of the *2s* orbital ends up with the formation of in-plane $2p_x$ and $2p_y$ orbitals which create sigma bonds, and the $2p_z$ orbital which is perpendicular to the plane and responsible for the π-bonds with neighboring atoms.

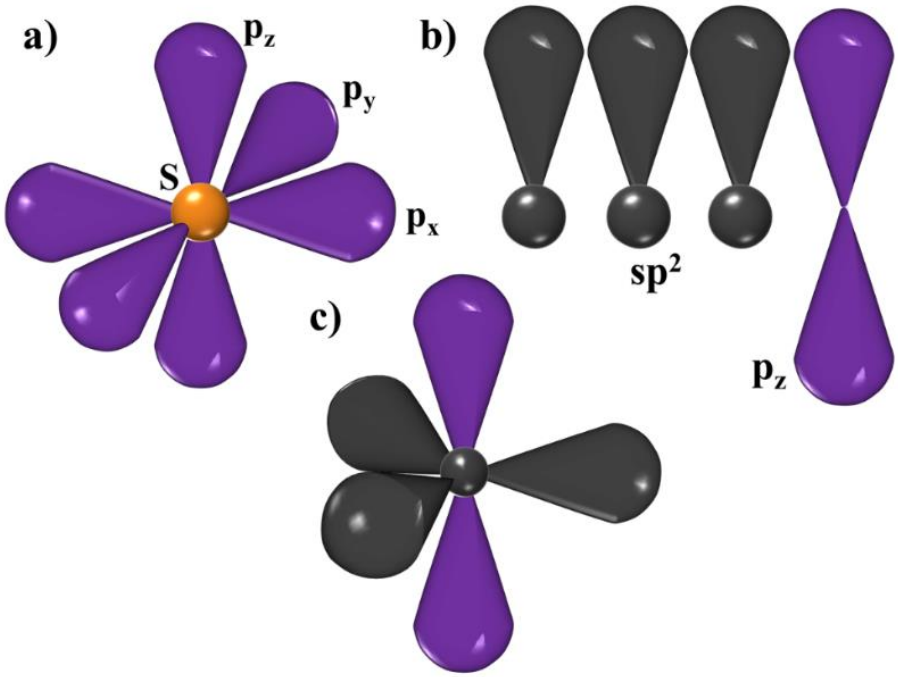

Figure 2.1. sp^2 hybridization of carbon. (a) carbon atom with *2s* and *2p* orbitals, (b) hybridization of carbon with three sp^2 orbitals and one p_z orbitals, (c) structural view of sp^2 hybridized carbon atom.

The reciprocal lattice of the honeycomb patterned infinite graphene sheet also gives a hexagonal lattice, in this instance it is rotated by 90° as seen in figure 2.1.

2.2. Electrical Properties of Graphene

The fact that graphene has a linear dispersion relation, which also signifies the independence of mobility from charge carrier density, close to the charge neutrality point, was theoretically shown by P.R. Wallace [26]. Long after the calculations, the experimental results verified [11] the theoretical model, hence the electrons in graphene were shown to obey relativistic Dirac equation instead of the Schrödinger equation.

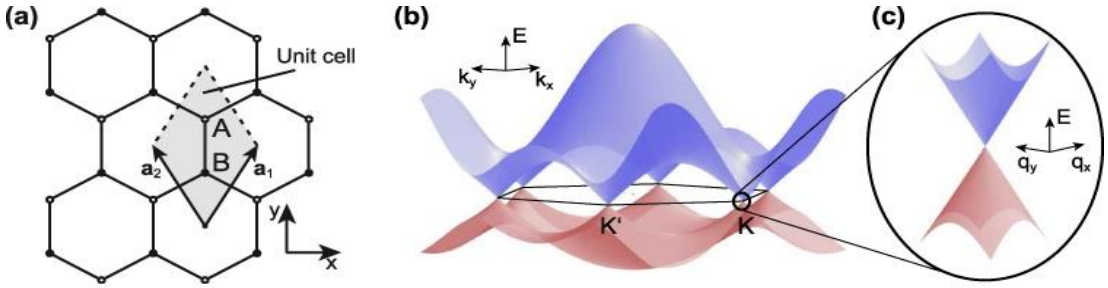

Figure 2.2. (a) Graphene lattice with two carbon atoms per unit cell denoted by A and B. (b) Electronic dispersion of graphene. The π-band (red) and the π*-band (blue) touch each other at singularity points (K and K' points). (c) Zoom of the dispersion at the singularity points. The dispersion has a conical form with an approximately linear slope. For more details about the band structure calculation see [27]–[29]. Figure is taken from [30].

The band structure of graphene can be calculated from the reciprocal lattice (figure 2.2) by using both ab initio [28] or tight binding methods [29]. The tight-binding calculations for the band structure proposes that;

$$E = \pm\sqrt{\gamma_0^2[1 + 4\cos^2\left(\frac{k_y a}{2}\right) + 4\cos\left(\frac{k_y a}{2}\right).\cos(\frac{k_x\sqrt{3}a}{2})]} \qquad (2.1)$$

where ± indicates the conduction and valance bands; γ_0 and a indicates nearest neighbor hopping energy and lattice constant of graphene and which are 2.8 eV and 2.46 Å respectively.

Tight-binding approximations for graphene, as seen in figure 2.2.b, show that contrary to semiconductors, graphene does not have a band-gap. The linear dispersion relation at the points K and K' also shown in figure 2.2.c; which is also known as high symmetry points of graphene.

$$E = \pm v_F \hbar |\vec{k}| \tag{2.2}$$

where v_F is the Fermi velocity. The situation which the Fermi level is below the Dirac energy represents p-doping of graphene, where the majority charge carriers are holes. Accordingly when the Fermi level is above the Dirac energy graphene becomes n-doped, whence the majority charge carriers become electrons. At absolute zero, there are no charge carriers present near K and K' points, thus this point is called the charge neutrality point.

The first electronic measurements on single layer graphene made by Novoselov *et al* [8] showed confounding characteristics that are unlike the observations made on typical semiconductors. The measurements also manifested that the electronic transport in graphene was governed by massless relativistic fermions with mobilities up to 1.5×10^4 $cm^2/V.s$ at low temperatures.

The theoretical limit on mobility which arises from the acoustic phonon scattering was found to be 2×10^5 $cm^2/V.s$ [31], [32] for planar graphene in no contact with either a substrate or the environment, at room temperature. Nevertheless the experimental results taken at low temperatures for suspended graphene exceeded the fore mentioned limit, with mobilities reaching up to 2.3×10^5 cm^2/Vs [33]. Lately, suspended graphene samples with mobilities up to 6×10^5 $cm^2/V.s$ are fabricated by Tombros *et al* [34]. Those abovementioned mobilities are more than 400 times higher than measured for silicon samples [35].

2.3. Optical Properties of Graphene

Optical conductivity (G) is authentically used to describe the optical properties of thin films. Two-dimensional (2D) Dirac spectrum with a conical dispersion relation is described as;

$$\varepsilon = \hbar v_F |\boldsymbol{k}| \tag{2.3}$$

where $v_F \approx 10^6$ m/s is the Fermi velocity and k is the wave vector. Theoretically, G is predicted [36]–[40] to have a universal value for the situations where photon energy is larger than both the Fermi energy and the temperature, given by;

$$G_0 \equiv \frac{e^2}{4\hbar} \tag{2.4}$$

All optical properties such as Transmission (T), Reflection (R) of graphene can be expressed by universal constant, given to the universal value of G. Kuzmenko *et al* [39] showed that for normal incidence of light;

$$T = (1 + 2\pi G_0/c)^{-2} = (1 + 0.5\pi\alpha)^{-2} \approx 1 - \pi\alpha \tag{2.5}$$

can be written in particular. By using directly observable quantities T and R, Geim *et al* [41] found T = 97.7% with an accuracy of ± 0.1 % for graphene membranes. For white-light region (450 nm < λ < 800 nm) the analysis for G yielded $G \approx 1.01G_0$ with a statistical standard error of ±4%.

For under 400 nm wavelengths, graphene still shows higher than 85% transmissions but as shown in figure 2.3 between 250 nm and 400 nm, graphene shows more opacity than other wavelengths. Geim *et al* [41] claims that this is because of graphene is contaminated by hydrocarbon materials during transfer processes. Usually photolithography materials which are highly sensitive for UV regime; are used for transferring graphene to dielectric substrates.

2.4. Electrode Applications of Graphene

So far the researches shows that graphene has proven itself to be an excellent candidate for transparent and bendable electronic device technologies. It is revealed by Kean Soo Kim *et al* [25] that graphene can be adopted to Polydimethylsiloxane (PDMS) substrate as a transparent electrode for possible flexible device applications. It is also shown by Wu *et al* [42] that graphene can be implemented on Organic Light Emitting Diodes (OLEDs) as a transparent conductive anode, which results in similar results

compared to conventional OLEDs with ITO, yet with reduced thickness of the optical stack.

In another report, Arco *et al* [43] illustrates a method to implement CVD grown graphene on continuous, flexible and transparent electrodes for organic photovoltaics (OPVs), which would result in significant improvements by means of producing transparent electrode for solar cells, due to the method's admissibility, scalability and affectivity.

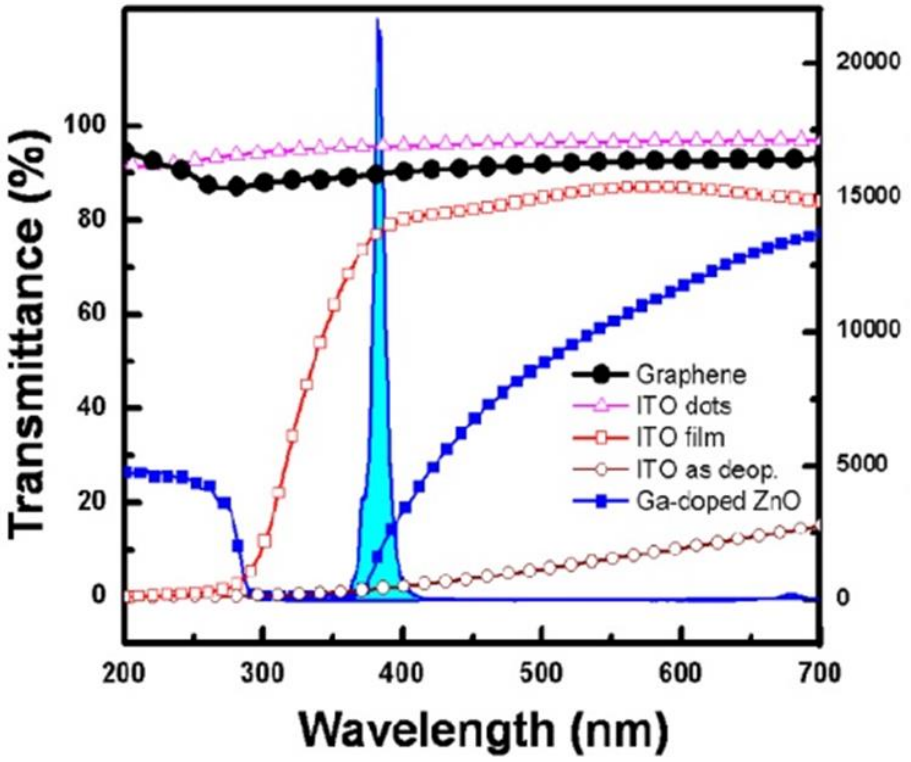

Figure 2.3. The optical transmittance of graphene, as-deposit ITO, annealed ITO, ITO nanodots and Ga-doped ZnO films, respectively, as a function of wavelength [18].

Patterned multi-layer graphene layers are also proven to be plausible to implement on large scale, batch fabricated GaN LEDs as transparent conducting electrodes. The work of Jo *et al* [44] have shown that the patterned multilayer graphene film which has more than 85% transparency between 400-800 nm wavelengths, possesses around 620 ohm/□ resistance.

2.5. Rectification at Graphene/Semiconductor Interface

In the last few years, the interface properties for graphene/semiconductor junctions have become the focus of many research groups. The strong Van der Waals interaction between the transferred graphene and semiconductor substrate gives rise to charge transfer across the interface and the formation of rectifying (Schottky) barrier. The electrical properties of graphene/semiconductor interface are sufficiently described by thermionic emission model and the Schottky-Mott model which is based on the bond polarization theory. The rectification at graphene/semiconductor interface can be utilized to sensors, which are exponentially sensitive to changes in the Schottky barrier height in forward bias, mainly because of the absorbates on the graphene, and also to analog devices where the Schottky barriers are integral components. The optical transparency, resistance to diffusion and mechanical stability make such graphene applications promising for future electronic devices.

2.6. Schottky-Mott model and Bardeen Limit

The ohmic or rectifying nature of the contact in the Schottky model for an ideal, intimate metal-semiconductor contacts are determined by the work functions of metal and semiconductor, φ_m and φ_s. The energy level diagrams for metal contacts n-type and p-type semiconductors are shown in figure 2.4 and figure 2.5 respectively [45]. Figure 2.4.b illustrates the metal contact to an n-type semiconductor, $\varphi_m > \varphi_s$ condition gives rise to a rectifying contact that barriers the flow of the electrons in each direction. The electrons that move from n-type semiconductor into the metal face with a barrier given by $\varphi_m - \varphi_s$, whereas the electrons moving from the metal to n-type semiconductor face with $\varphi_m - \chi_s$. Here, the χ_s parameter is defined as the electron affinity of the semiconductor. When the n-type semiconductor is kept negative with respect to metal, that is to say, in forward bias conditions, the forward barrier reduces to $q(V_b - V_a)$, where V_b defines the bias potential and V_a the applied voltage. Nevertheless the barrier to the reverse flow is not affected by the bias voltage and it is described as the barrier height (φ_{bh}) for the metal-semiconductor interface as;

$$\varphi_{bh} = \varphi_m - \chi_s \tag{2.6}$$

Figure 2.4.d shows that for $\varphi_m < \varphi_s$ condition in a metal to n-type semiconductor contact there exists virtually no barrier; under this circumstance the contact is said to be ohmic.

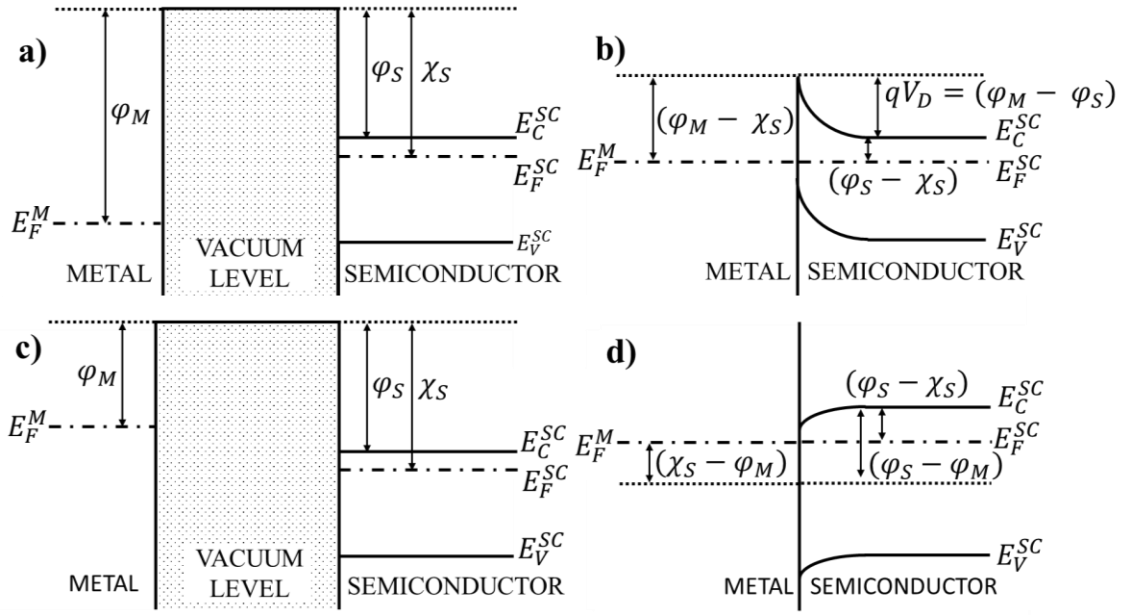

Figure 2.4. Energy-band diagram of a metal contact on a n-type semiconductor [45].(a) and (c) illustrates metals with two different fermi level, respectively, and n-type semiconductor before the physical contact with each other. (b) and (d) illustrates band bending of semiconductors after the physical contact with metal.

Figure 2.5 displays the band diagrams for metal contact on p-type semiconductor. Under $\varphi_m < \varphi_s$ condition the hole flow is restricted by a barrier of height $(\varphi_s - \varphi_m)$, thus the contact shows rectifying character. Under forward bias condition, where p-type semiconductor is kept positive with respect to metal, the barrier decreases, yet the barrier for reverse bias is constant and it is described to be the barrier height.

$$\varphi_{bh} = E_G - (\varphi_m - \chi_s) \tag{2.7}$$

For $\varphi_m > \varphi_s$ condition, there is no barrier for the current flow, thus the contact becomes ohmic.

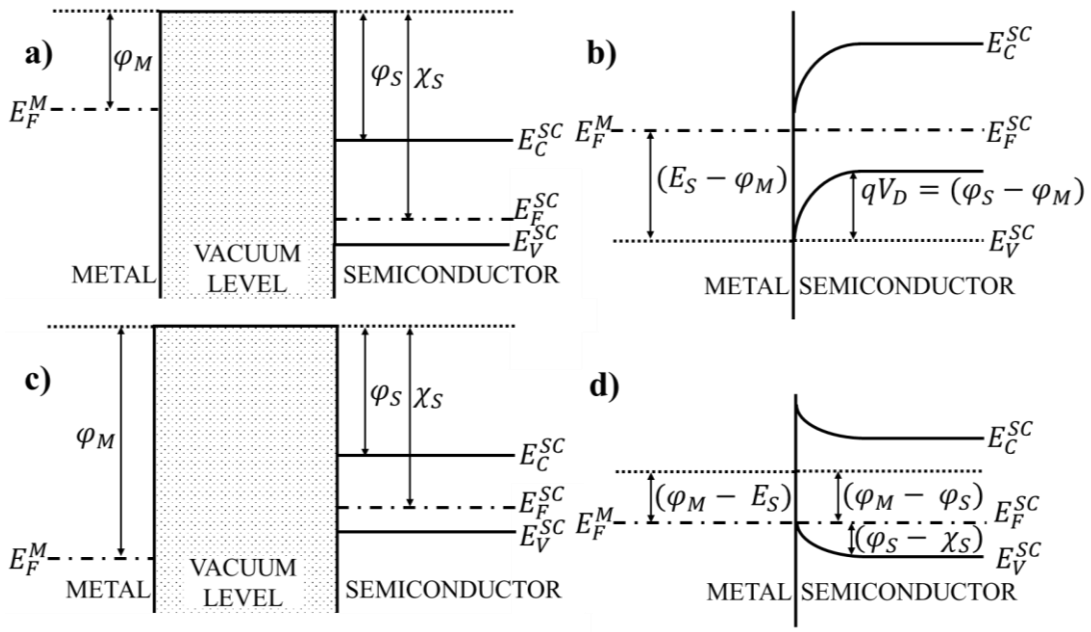

Figure 2.5. Energy-band diagram of a metal contact on a p-type semiconductor [45].(a) and (c) illustrates metals with two different fermi level, respectively, and p-type semiconductor before the physical contact with each other. (b) and (d) illustrates band bending of semiconductors after the physical contact with metal.

The barrier height for metal-semiconductor junction, also known as the Schottky Mott limit [46], is independent of both applied bias and the doping. When the φ_{bh} value is positive, the contact shows a rectifying character and is called the Schottky barrier height (SBH). On the other hand, when there is an ohmic contact, φ_{bh} gets a small negative value also known as the dipole surface charge barrier. Equation 2.6 and 2.7 manifests that for the same metal, for any given semiconductor, the sum of the barrier heights in n-type and p-type materials should be equal to the bandgap of semiconductor. For ideal metal-semiconductor junction, Schottky-Mott model manifests that SBH should be dependent on the metal work function linearly.

2.7. Charge Transport Processes

The current transport in metal-semiconductor contacts is mostly governed by the majority charge carriers, unlike the minority charge carriers are responsible in p-n junctions. Four fundamental transport processes can be seen on figure 2.6 under forward bias, the reverse processes occur in case of reverse bias [47]. Those processes are (1) electron emission from the semiconductor over the potential barrier to the metal (this

process is known to be dominant for moderately doped semiconductors under moderate temperatures), (2) quantum-mechanical tunneling of electrons through the barrier which is critical for heavily doped semiconductors and responsible for ohmic contacts, (3) recombination of the charges, just as observed in a p-n junction, (4) electron diffusion in depletion region. For high mobility semiconductors the transport can be described by the thermionic emission theory.

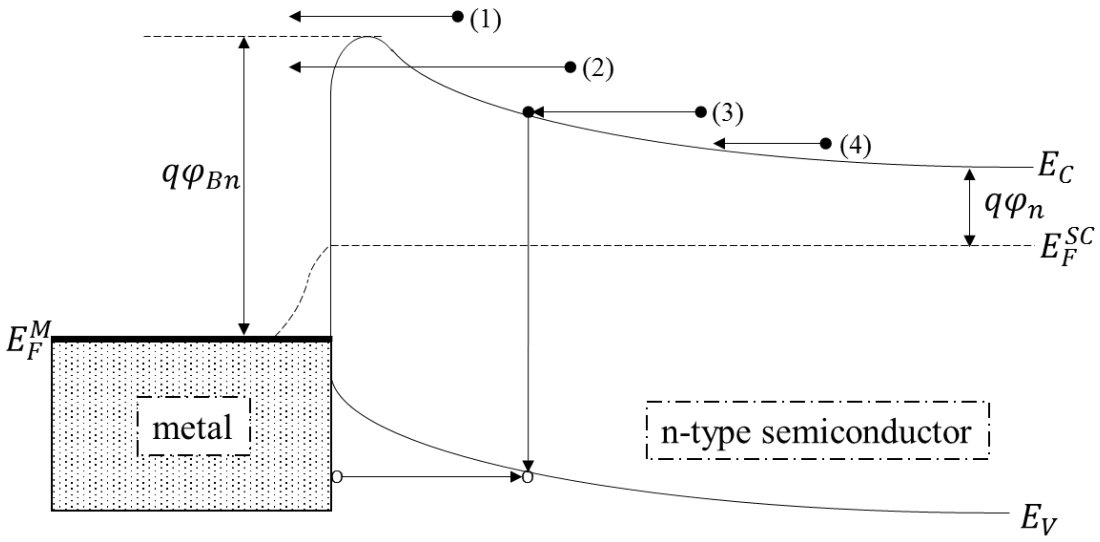

Figure.2.6. Four different basic transport processes under forward bias. (1) Thermionic-emission. (2) Tunneling. (3) Recombination. (4) Diffusion of electrons.

2.8. Thermionic Emission Theory

The thermionic emission theory indicates that only electrons which have enough energy to pass barrier on top of it, can contribute to the current. Current flow which is not affected by shape of the barrier, is only dependent on barrier height. The theory assumes certain conditions as follows (1) the barrier height of the system is much higher than thermal energy of system, (2) system is thermally equilibrated at the interface and (3) thermal equilibrium does not affected by charge accumulation at the interface [49].

For the sake of simplicity current density across the metal/semiconductor interface can be derived as;

$$J(T,V) = J_S(T)\left[exp\left(\frac{qV}{\eta k_B T}\right) - 1\right] \tag{2.8}$$

where Js(T) is saturation current and can be described as $J_S = A^* T^2 exp\left(-\frac{q\varphi_{SBH}}{k_B T}\right)$ and η is ideality factor. A* is area of junction, T is temperature, k_B is Boltzman constant. The derivation of current density already done elsewhere and it is not the subject of this thesis [50].

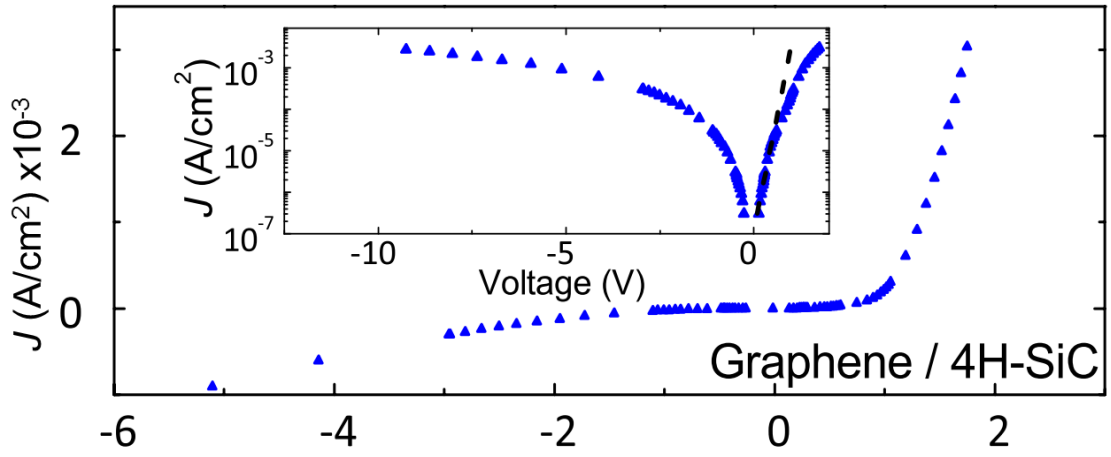

Figure.2.7. Room-temperature current-density-voltage characteristics show Schottky rectification at the graphene/n-4H-SiC interface. Inset shows Semi-logarithmic plots of J-V [48].

2.9. Schottky Contact Between Graphene/Semiconductor Interface

Tongay *et al.* [48] showed that transferring CVD grown graphene on different semiconducting materials such as n-type Si, GaAs, 4H-SiC and GaN, results in rectifying Schottky character at the metal-semiconductor interface. Figure 2.7 shows J-V data for graphene/4H-SiC junction that show a strong rectification character, which is a consequence of the Schottky barrier formed at the interface, because the electrons flow from semiconductor to graphene until the Fermi energies are aligned.

They also conducted temperature dependent measurements for the same four different junctions and results manifest that for both bias directions, as the temperature increases larger current flows and the probability of a conduction electron overcoming the potential barrier increases. In contrast, as the temperature is decreased, smaller current flows and the probability for the conduction electron to overcome the potential barrier decreases. SBH value can be obtained directly from the slope. The obtained Schottky barrier heights are 0.86 eV, and 0.91 eV for Si, and 4H-SiC, respectively.

CHAPTER 3

SILICON CARBIDE (SiC) AND EPITAXIAL GRAPHENE

3.1. Silicon Carbide

SiC is a wide gap semiconductor which was firstly synthesized in the 19th century. Due to its wide bandgap, high thermal conductivity and extreme mechanical robustness, SiC has been a hotspot of research for devices that work under extreme conditions such as high temperature, high power and high frequency, where it is impossible to implement other semiconductors such as Si or GaAs. SiC is also found to be resistant for high doses of radiation, whence making the usage of SiC in nuclear power applications desirable. Owing to its wide bandgap, SiC is also implementable to the optical devices that operate under blue and UV light, such as photodetectors. Although the significant properties of SiC has led to an adequate amount of fundamental research in the last few decades, the number of commercialized SiC based devices remained low due to low-quality samples and unsatisfactory epitaxial processes.

SiC is known to have several hundreds of polytypes, ranging from purely cubic crystal structure (3C-SiC) to purely hexagonal structure (2H-SiC), albeit it has only three topmost mentioned polytypes, namely 3C-SiC, 6H-SiC and 4H-SiC. The first polytype commercially available as single crystal was 6H-SiC, followed by 3C-SiC, which could be obtained epitaxially by deposition on Si substrates – yet the quality of 3C-SiC bulk crystals grown by this method have low quality. Lastly, the advancements on the growth method of 4H-SiC bulk crystals bared fruit and high quality 4H-SiC wafers which have higher mobility compared to 6H-SiC samples probably due to lower and more isotropic effective masses, became available. 4H-SiC polytype is known to have a band gap of 3.23 eV that is higher than those of 6H-SiC and 3C SiC at 300 K, which are 3 eV and 2.36 eV [51], respectively.

There are many device applications based on SiC. One example could be the high-frequency SiC-based devices which delivers continuous high power at X-band (8-10 GHz) at high temperatures, up to 500 °C, which is highly applicable to radar and

communications systems for unpiloted aerial devices and distributed satellite arrays. Sensors that can operate over 300 °C needed for the processes under harsh environments are needed for petroleum industry where the need could be satisfied by SiC-based devices [52]. Engine control sensors and various other parts in automotive industry can also be manufactured by using SiC. By the adding different impurities to SiC, it is possible to acquire an electro-luminescent material across the entire visible spectrum, despite of its indirect bandgap, which allows SiC to be used in a wide variety of optical devices. Due to its large bandgap, it is also plausible to implement SiC to photodetectors that operate in the UV spectrum range.

The commercial availability of SiC led to technological advances in the processing technology rapidly, followed by demonstrations such as integrated circuits, complementary metal-oxide-semiconductor (CMOS) analog integrated circuits [53], nonvolatile random-access memories [54], self-aligned polysilicon-gate metal-oxide-semiconductor field-effect transistors (MOSFETs) [55]and buried-channel polysilicon-gate charge-coupled devices (CCDs) [56].

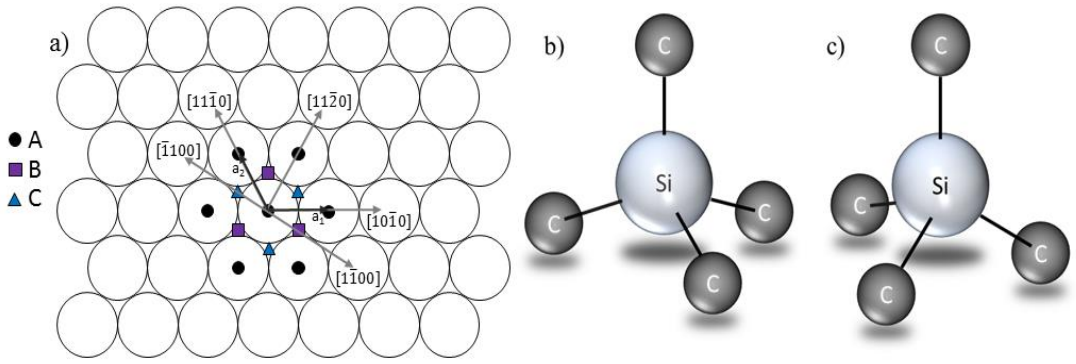

Figure 3.1. (a) A close-packed hexagonal plane of spheres, with centers at points marked A. A second and identical plane can be placed atop the first plane, with centers over either the points marked B or the points marked C. (b) The basic structural unit in SiC is a tetrahedron of four carbon atoms with a silicon atom in the middle. (c) A second type rotated 180° around the stacking direction, with respect to the first type of tetrahedra, can also occur in SiC crystals.

3.2. SiC Polytypes: Structure and Symbolic Notations

Polytypism is one-dimensional polymorphism which is known to be possessed by SiC, the only known binary compound of these elements. Polytypic compounds are

known for having similar sheets of atoms or symmetrical variants stacked on top of each other with a relation to a symmetry operator. Thus the difference between the polytypes arises only from the differences found in c-axis, which is perpendicular to the sheets. The sheets can be thought of as a close pack array of spheres forming a two-dimensional pattern with six fold symmetry, which is in SiC case bilayers composed of one layer of Si and one layer of C atoms. Figure 3.1 illustrates the first sheet as the basal plane with Miller indexes in form of hexagonal crystal structure. In order to stably stack the planes on top of each other, the second sheet must be either placed in the valleys between the atoms, such as along $[\bar{1}100]$, denoted as "B" or along $[1\bar{1}00]$, denoted as "C" in figure 3.1. Consequently, the sheets can be named due to the placements of their spheres, and all the prototypes possess a different sequence of sheets A, B and C. The only restriction here is that sheets with same displacement, hence possessing the same letter, cannot go on top of each other.

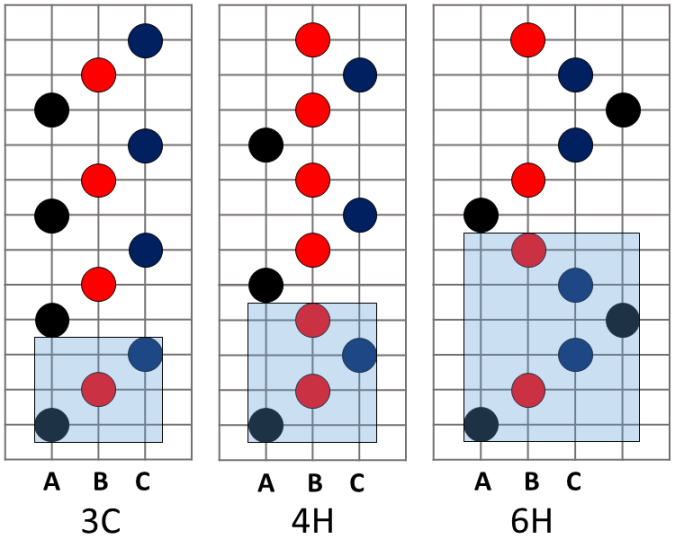

Figure.3.2. Stacking sequence for 3C, 4H and 6H-SiC, respectively.

The structural unit for all SiC polytypes is a tetrahedron, consisting of four carbon and one silicon atoms at the center, that are 88% covalent, 12% ionic bonded (figure 3.1.b). Approximately, the bond length between C-C and Si-Si atoms are found to be 3.08 Å where the bond length of Si-C atoms is 1.98 Å. In order to form a SiC crystal, these tetrahedral molecules are assemble with each other at the corners, and the stacking notations represent Si-C bilayer sheets. The tetrahedral structure is three-fold symmetric around the axis parallel to the stacking direction. Thus secondary types of sheets are obtained by turning the tetrahedral molecules by 180^{o} with respect to their initial states,

along the symmetry axes. Those sheets are named A', B' and C', and referred as "twinned" where the initial type of tetrahedra are called "untwinned".

According to some sources more than 250 types of SiC polytypes can be found in the nature [57], some of them having a stacking sequence of several hundreds of bilayers. SiC polytypes have three different crystal structures, cubic, also referred as β-SiC, hexagonal and rhombohedral, both also referred as α-SiC. Ramsdell [58], proposed that the polytypes should be named according to the periodicity number of their stacking sequence and the type of their crystal; H for hexagonal, C for cubic and R for rhombohedral (figure 3.2).

The wurtzite 2H structure, with a stacking sequence ..AC'AC.. along [0001] direction and the zinc-blende 3C structure with a stacking sequence ..ABCABC.. along [111] direction are the simplest stacking sequences for Si-C bilayers. Even though the wurtzite and zinc-blende are most common structures among the binary octet semiconductors, the wurtzite structure is rare for SiC. The properties of the most common polytypes of SiC, namely 3C, 4H, 6H and 15R, are summarized in Table 3.1 and the stacking sequences for 3C, 4H and 6H are shown in figure 3.3 for $(1\bar{1}0)$, $(11\bar{2}0)$ and $(11\bar{2}0)$ planes respectively.

Table.3.1. Specific parameters for 4H [59], 3C and 6H [60] SiC.

Ramsdell	**3C**	**4H**	**6H**
Structure	Zinc-blende	Wurtzite	Wurtzite
Type	β	α,III	α,II
ABCA'B'C'	…ABC…	…ABA'C'…	…ABCB'A'C'…
Hexagonality	0%	50%	33.3%
Atoms/unit cell	2	8	12
a(Å)	3.08	3.08	3.08
c(Å)	7.55	10.05	15.12
V ($Å^3$)	62.14	82.32	124.24
d (g/cm^3)	3.21	3.24	3.22
Band gap (eV)	2.36	3.23	3

3.3. Physical Properties of SiC

One of the most outstanding properties of SiC is its durability in high temperatures, which makes the applications of this substance a reliable candidate for high-

temperature electronic applications. It also higher thermal conductivity for 300 K and higher temperatures than Germanium and Silicon [61].

SiC polytypes are known to have indirect, yet different bandgaps rising due to the rise in its degree of hexagonality. This phenomenon leads to slight changes in the optical properties of SiC polytypes. As shown in figure 3.3; due to its 3.23 eV band gap 4H-SiC can absorb all wavelengths between 200 nm and 380 nm.

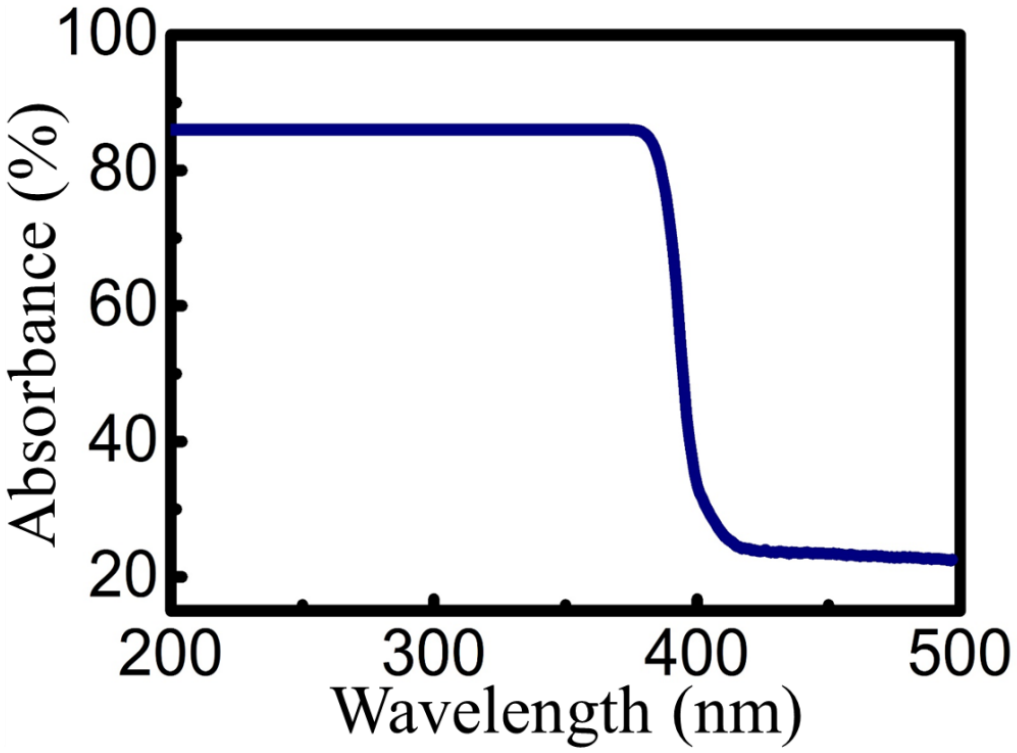

Figure 3.3. UV-Vis absorption spectrum of 4H-SiC.

It is possible to acquire n-type SiC polytypes by doping nitrogen or phosphorus as donors and p-type SiC by doping boron, aluminum or gallium as acceptors. Ordinarily, the SiC samples are n-doped due to the presence of nitrogen during crystal growth processes. Donor and acceptor levels for 3C, 4H, 6H, 15R and 33R polytypes are presented for nitrogen and aluminum in ref [62] and for nitrogen, aluminum, gallium and boron in ref [63]. The charge carrier mobilities in SiC are dependent on the temperature and the nature of the sample, such as carrier concentration, structural quality and polytype. For unintentionally doped samples, a decrease in residual carrier concentrations and an increase in mobilities are observed. A compilation of mobility data for 3C, 4H, 6H and 15R polytypes under various conditions are given in ref [63]. SiC is a desired

candidate for high-power and high-frequency devices owing to its high break-down electric field and high saturated electron drift velocity.

The sum of the forementioned thermal, optical and electrical properties of SiC can be seen on Table 3.2 for the most common polytypes of SiC.

Table 3.2. Thermal, optical and electrical properties of SiC for different polytypes. Data taken from ref [64].

Polytype	Property	Value	Comments
4H-SiC	Thermal conductivity (W/cm.K)	4.9	RT
6H-SiC	Thermal conductivity (W/cm.K)	4.9	RT
4H-SiC	Saturated electron drift velocity (cm/s)	$2.0x10^7$	RT
4H-SiC	Electron mobility @10^{16} cm^{-3} (cm^2/V.s)	800	RT
4H-SiC	Hole mobility @10^{16} cm^{-3} (cm^2/V.s)	115	RT
6H-SiC	Saturated electron drift velocity (cm/s)	$2.0x10^7$	RT
6H-SiC	Electron mobility @10^{16} cm^{-3} (cm^2/V.s)	370	RT
6H-SiC	Hole mobility @10^{16} cm^{-3} (cm^2/V.s)	90	RT

3.4. ITO and Ni Electrodes on SiC

MSM junctions are one of the most popular structures for photodetector applications. Compared to the p-n junction type photodetectors, MSM photodetectors have much smaller capacitances, lower response times and faster operation speeds. The key idea behind these devices is finger like interdigitated electrode formations on the photo active material. Metal electrodes like Ni on 4H-SiC yield low dark current due to elevated Schottky barrier height and show a 5 order of magnitude difference between dark current (figure 3.4.a) and photo current (figure 3.4.b) [14]. However most of the incoming light is blocked by the metal electrode due to its low transmission profile in UV and visible range (figure 3.4.c). On the other hand, in the same research ITO transparent electrodes provided improved optical properties but dark current of the devices is extremely large due to lower Schottky barrier height between ITO and 4H-SiC.

Graphene is a better alternative to metal and ITO electrodes possessing a relatively high Schottky barrier (figure 2.7) and favorable optical properties (figure 2.3) as explained in the previous chapter.

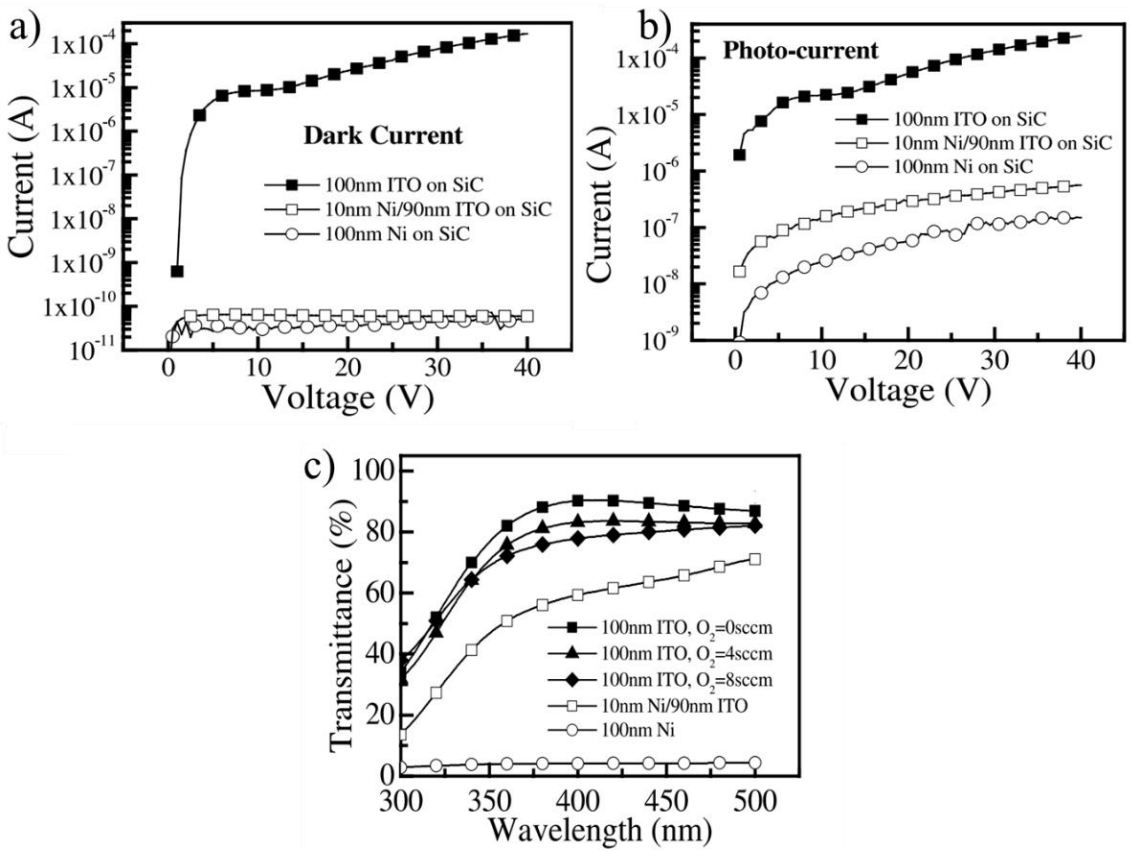

Figure 3.4. (a) Dark I-V and (b) photo I-V characteristics for the SiC MSM UV photodetectors with 100 nm ITO, 10 nm Ni/90 nm ITO and Ni as the material or contact electrodes. (c) Optical transmittance measurements of same contact materials. Figure is taken from [14].

3.5. Epitaxial Graphene Contact Electrode for SiC

One atom thick graphene layer can be grown readily on UV sensitive SiC substrate by high temperature vacuum annealing process, needless of any deposition and/or transfer method [22], [65], [66]. SiC stands out owing to its wide band gap and advanced material characteristics as discussed in previous sections for the fabrication of UV photodetectors that work under harsh environments [67]. SiC, which is a visible-blind material as mentioned below, shows low leakage currents and high responsivity between 200-400 nm even at high temperatures.

Similarly, a Schottky barrier is reported at the interface of epitaxial graphene and SiC substrate [68]. Single layer graphene exhibits a work function of φ_G= 4.5 eV on 4H-SiC substrate that has an electron affinity of χ_e= 3.3eV [69]. Here, Schottky-Mott model predicts a SBH (φ_{SBH}) of 1.2 eV, due to definition $\varphi_{SBH} = \varphi_G - \chi_e$. The theoretical value agrees well with the experimentally obtained value of φ_{SBH} = 1.06+-0.14 eV [68]. Abovementioned facts predicts the epitaxial graphene/SiC heterojunction to have a strong rectification character, which can be adapted to Schottky barrier devices such as tunneling field effect transistors and UV photodetectors with low leakage currents.

CHAPTER 4

GROWTH AND CHARACTERIZATON OF EPITAXIAL GRAPHENE ON SIC

4.1. Epitaxial Graphene Growth Setup

Ultra high vacuum (UHV) is essential for researches that needed to be conducted under almost space like vacuum environments. Obtaining such a high vacuum environment requires specific equipment and baking process, which is acquired by keeping entire system above 100 ^{o}C for hours to remove water and gas molecules that were adsorbed in the inner surface of the vacuum chamber.

In this study, all the experiments were conducted in our UHV system that is crucial for the growth of epitaxial graphene. Some special, initial procedures must be met to achieve UHV condition in a chamber. At the start, a dry pump is used as the roughing pump, which cleans the chamber from small particles such as dust and takes the system down to a pressure of about 10^{-2} mbar. When the system reaches to 10^{-2} mbar or even a bit lower, turbo-molecular pump is turned on to reach the UHV level, that process takes the pressure in the chamber down to low 10^{-10} mbar range. The UHV chamber and its components that we used during our experiments are shown in figure 4.1. The base pressure of UHV chamber is shown in figure 4.1.c which measurement taken from IMG and cold cathode (Aux1) gauges. In figure 4.1.c pressure values different from each other because 10^{-10} mbar is out of range of cold cathode gauge.

Due to the high temperatures during the annealing process, we designed and fabricated special sample holder consists of special parts (figure 4.2). Whereas the outer parts are stainless steel, the inner parts are made of heat-proof materials such as Tantalum (Ta) and Alumina Ceramic (Al_2O_3). Both of these materials are frequently desired for high temperature applications, owing to their high melting points, given as 3020 °C and 2072 °C for Ta and Al_2O_3, respectively. Given to its excellent dielectric property, Al_2O_3 here is used to isolate Ta plates from each other to avoid any shortcut in the system. The sample stage during annealing process can be shown in figure 4.2.d.

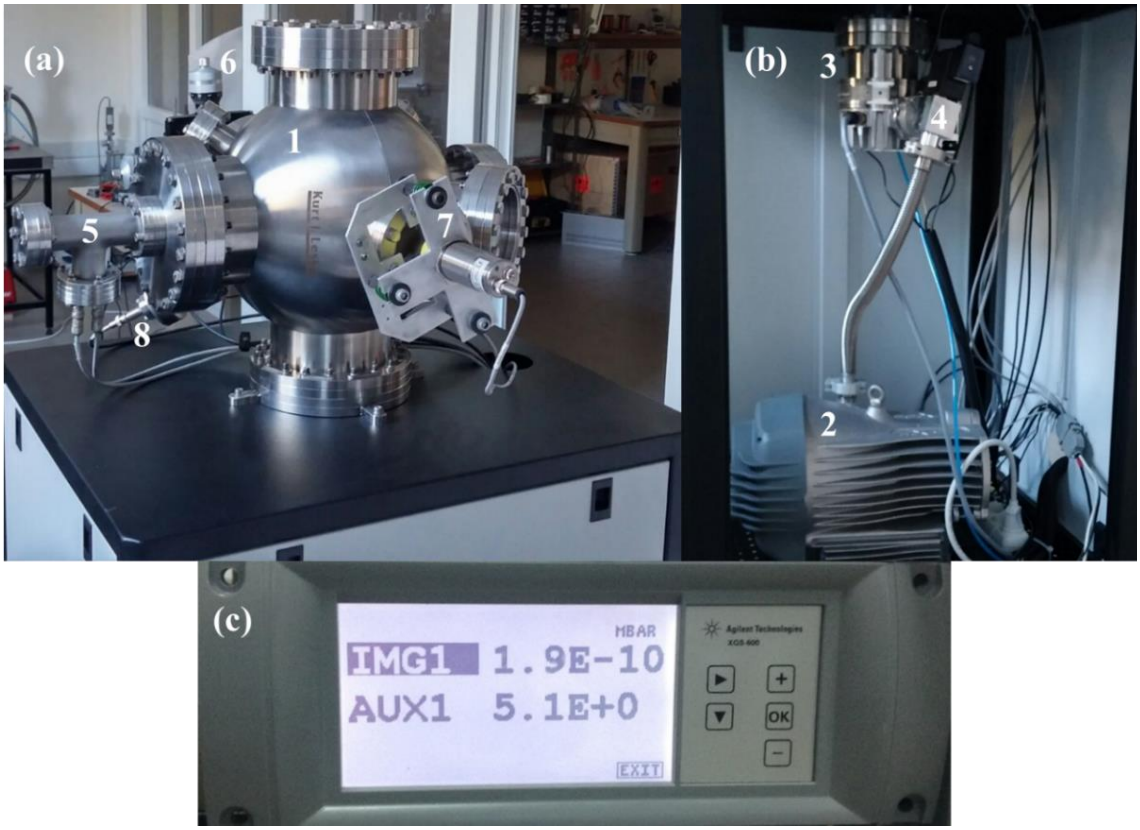

Figure 4.1. (a) and (b) epitaxial graphene growth setup. (1) UHV Chamber, (2) Edwards nxds6i scroll pump, (3) Turbo Molecular Pump, (4) Isolation valve, (5) Feedthrough where the sample holder is attached, (6) XYZ manipulator, (7) Optical pyrometer, (8) UHV vacuum gauge (Varian IMG-300). (c) Base pressure of UHV chamber.

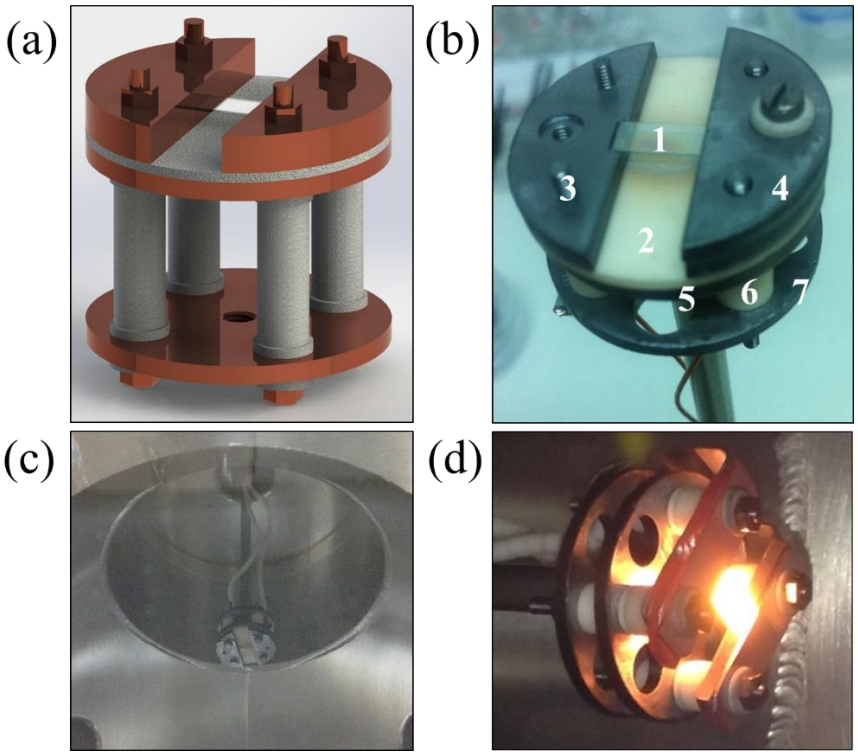

Figure 4.2. (a) 3D modelling of SiC annealing system, (b) SiC annealing system, (1) SiC substrate, (2) and (6) Al_2O_3 plate and beads, (3), (4), (5) and (7) Ta screws, nuts and plates, (c) SiC annealing system inside the vacuum chamber, (d) SiC annealing system at 1050 °C.

4.2. Growth Procedure

Experiments are conducted by using 250 μm thick, SI 4H-SiC wafer. A 2" wafer is obtained from NovaSiC and diced into 4x10 mm^2 parts. Before the growth process, the sample is chemically cleaned by acetone, isopropanol and deionized (DI) water. The native oxide layer present on the sample is removed by a 6% hydrofluoric acid (HF) solution.

The growth processes are carried out under UHV conditions with a base pressure of $2x10^{-10}$ mbar. Before the growth process, a 210 μm thick n-type 6H-SiC is graphitized by direct current heating and put on top of a SI 4H-SiC sample. Thanks to inert structure of graphite on 6H-SiC, it is possible to avoid from welding of two SiC together during annealing process. The graphitized SiC is essential for graphene growth on semi-insulating SiC because, as indicated in figure 4.3, due to the relatively high resistance of SI 4H-SiC, the current passes through only the n-type 6H-SiC. By virtue of Joule-Thompson heating principle, it is possible to heat 6H-SiC substrate up to 1500 °C, thus

also heating 4H-SiC sample up to 1500 °C due to the capping. The temperature during the annealing procedure is controlled by an optical pyrometer with ±1 °C resolution.

Before the growth process, we degassed each sample overnight at a temperature around 600 °C and removed the remaining surface oxide thermally by annealing the sample for 10 minutes at 1100 °C. Then the sample was annealed at 1500 °C for 5 minutes for the growth. The maximum chamber pressure is observed to be $8x10^{-7}$ mbar during the growth experiment.

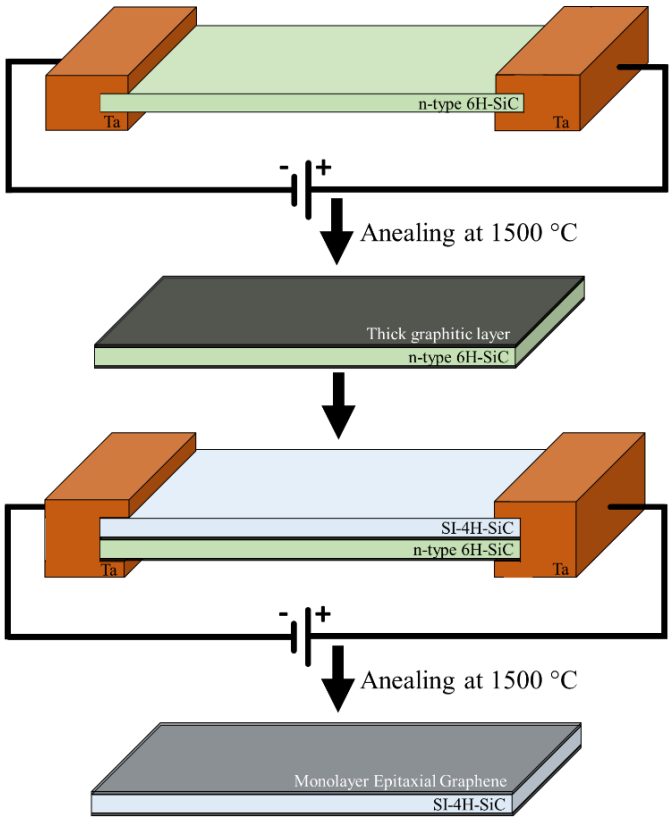

Figure 4.3. Schematic view of sample annealing mechanism comprising direct current heating and capping methods.

4.3. Atomic Force Microscopy Analysis

The morphology of the annealed sample surface is analyzed by atomic force microscopy (AFM) measurements, and then the results were compared to the ones obtained from as-received SiC surface. AFM images obtained after the annealing process show 2-5 μm wide-step terraces separated by oblique step edges with heights range depending on the width of the terrace (figure 4.4). The modification of the surface

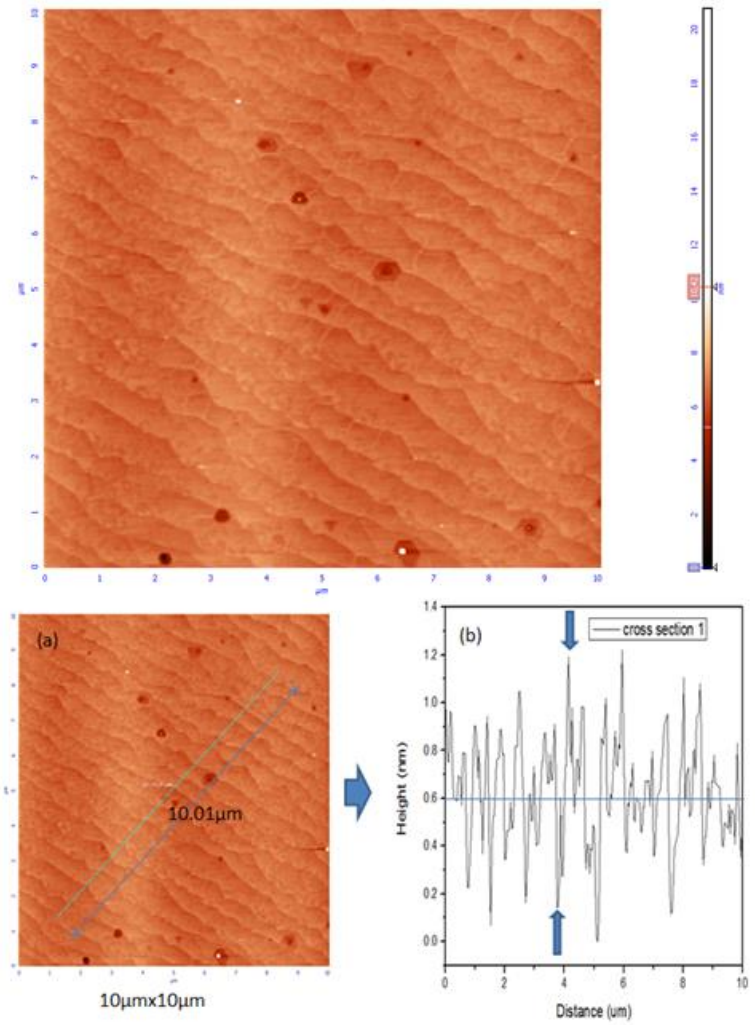

Figure 4.4. (a) AFM topography measurement of epitaxial graphene on SiC substrate. The measurement was taken from randomly selected 10 µm x 10 µm area. (b) AFM topography line profile measured along the stepped terraces on annealed 4H-SiC surface. (c) The height profile which corresponds to the cross section taken in (b).

does not arise from the formation of the graphene but from the annealing of SiC crystal that is described elsewhere [70]. Other from terraces, some dark spots are observed. These spots can be described as defects on SiC substrate. These defects may be act like nucleation center during annealing process for graphene growth.

The height of the terraces were determined by the subtraction of the minimum value of the signal from the maximum value of AFM. As an example, the measured height of a signal terrace shown in figure 4.4.b and c is found to be approximately 1.05 nm by the subscription of the minimum and maximum values of the AFM signal. These analyses presented us that the average height of each terrace is approximately 0.6 nm.

4.4. Raman Spectroscopy Analysis

Before the fabrication of the electrodes, a series of single point Raman spectroscopy measurements were taken from randomly chosen spots of the sample. Figure 4.5.a shows the observed graphene related D, G and 2D band peaks together with SiC background signals, which appear at 1520 cm^{-1} and 1713 cm^{-1}. The crystalline defects in the graphene matrix causes the D peak at 1368 cm^{-1} have relatively low intensity. Peaks at 1597 cm^{-1} and 2730 cm^{-1} wavenumbers respectively correspond to G and 2D peaks, which presents off-plane and in-plane optical phonon modes, respectively. The intensities of both G and 2D peaks do not vary with the position, suggesting that the thickness of the graphene is the same throughout the sample.

I_{2D}/I_G ratio is a powerful method to characterize thickness of graphene layer. It is known that for monolayer graphene I_{2D}/I_G ratio is equal or bigger than 2. The thicker the graphene layer results the lower the I_{2D}/I_G ratio. On the other hand, it is hard to distinguish G peak of graphene from SiC background signal for epitaxial graphene on SiC.

The number of graphene layers in our sample is quantitatively determined by attenuation method, which is discussed further in the reference [71]. In this method, the substrate's attenuation fraction defined as $e^{-2\alpha t}$ is extracted by the subtraction of a scaled reference spectrum of bare SiC sample from the obtained Raman spectrum of epitaxial graphene grown on SiC wafer. Here, the relative extinction coefficient is obtained experimentally and given by $\alpha = 0.02 \pm 0.002$, whereas the number of graphene layers in

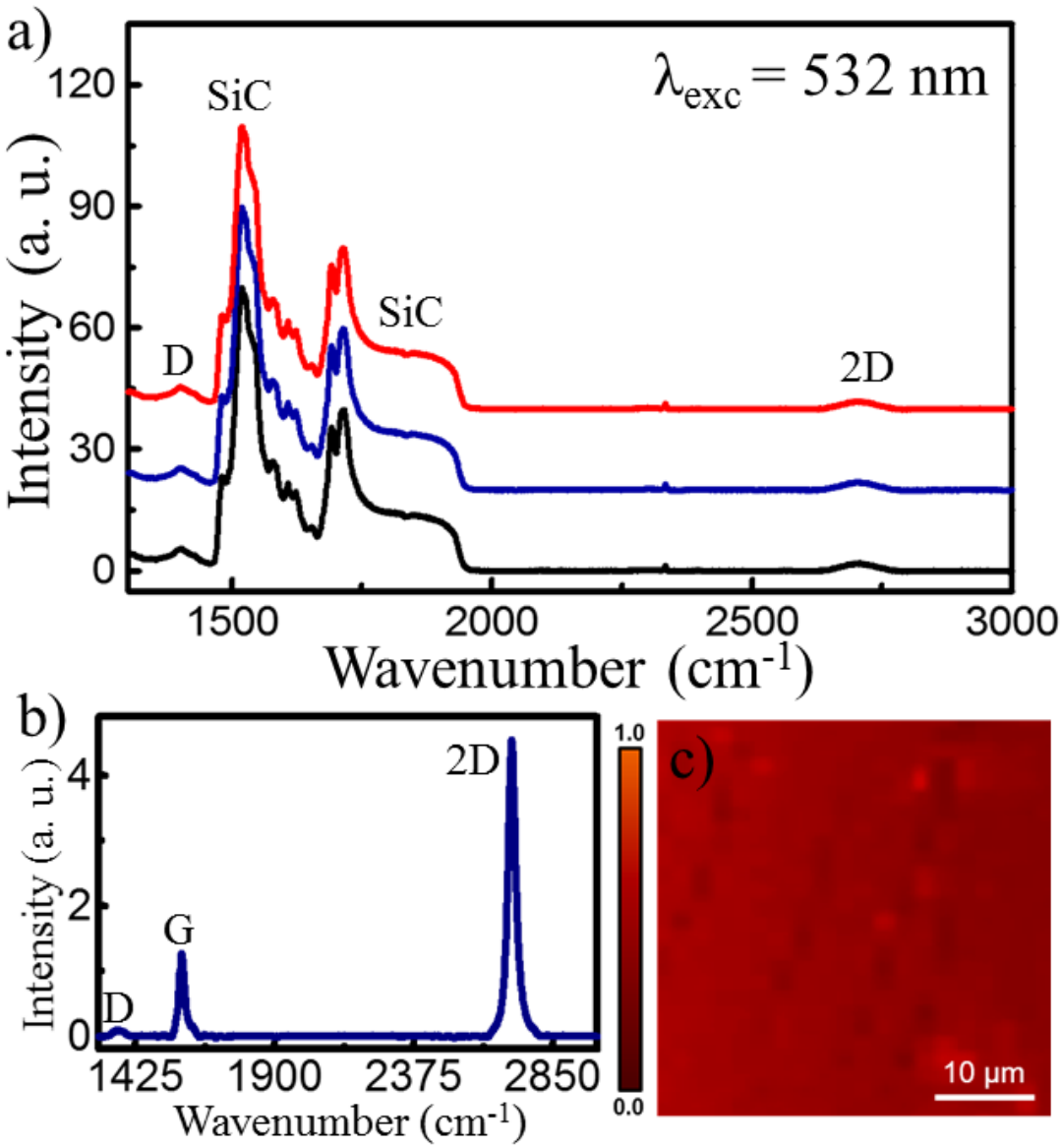

Figure 4.5. (a) Raman measurements of epitaxial graphene with SiC background signal which were taken from three different spot. (b) Raman signal of epitaxial graphene after attenuation method is applied. (c) Large area (35 μm x 35 μm) integrated 2D band intensity Raman map of the monolayer epitaxial graphene on SiC.

monolayer unit is given by t. Figure 4.5.b presents the result of SiC induced background subtraction from single point Raman measurements. The Raman profile obtained from this subtraction exposes the characteristic G and single Lorentzian 2D peaks, which are similar to those of mechanically exfoliated monolayer graphene on a 300 nm SiC substrate. The good graphitic quality is revealed by the strong G peak and the weak D peak which can be shown in figure 4.5.b and the monolayer nature of the epitaxial graphene is revealed by the large 2D to G (I_{2D}/I_G) peak intensity ratio which is in our chase bigger than 2.

A large area micro-Raman mapping of the 2D band intensities for a spectral range between 2500 cm^{-1} and 2900 cm^{-1} are also performed to verify the thickness uniformity. The laser used had an excitation wavelength of 532 nm and the map data is recorded by raster scanning mode with a precision two-dimensional stage having 1 μm step size. The homogeneity of the epitaxial layer is inferred by the 2D peak intensity distribution, which is shown in figure 4.5.c. The 2D peak intensity variation $\sigma(I_{2D})$ is calculated from the Raman map measurements, which is shown to have a value of 4%, revealed better results than that of few layer epitaxial graphene reported in reference [71]. We believe that unintentional weak fluctuations in the laser power might cause such small variations in the 2D peak intensity throughout the sample.

4.5. UV-Vis Spectroscopy Analysis

As we know, SiC based photodetectors show magnificent spectral response especially at the wavelength range of 200-380 nm owing to high optical absorption characteristics of SiC, and are not sensitive to UV radiation outside this region [67], [72]. Thus the optical UV-Vis absorption spectrum of bare 4H-SiC wafer is compared to the optical UV-Vis absorption spectrum of the 4H-SiC sample with epitaxial graphene, to determine whether the presence of grown epitaxial graphene has any impact on the UV absorption level of the SiC wafer. The measurements via UV-Vis spectrometer, shown in figure 4.6, are performed for wavelength range between 200-500 nm. As figure 4.6 presents, near 380 nm wavelength, the absorption of the both samples decreases sharply, due to the fact that the wavelength corresponds to the optical absorption edge of 4H-SiC, with a 3.26 eV wide energy band gap. Those measurements already imply that presence of epitaxial graphene has no significant effect on the UV absorption for the wavelengths

below 380 nm. Therefore we can conclude that epitaxial graphene can be used readily as a transparent material on SiC, without any disturbance on its high photo absorption level in the UV region.

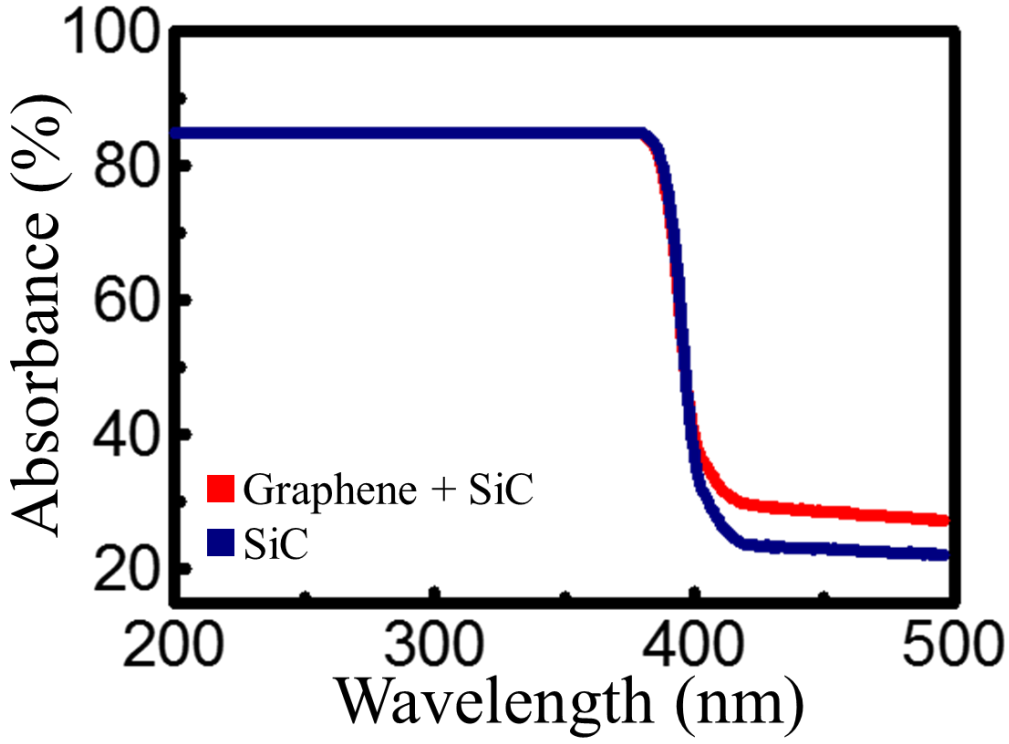

Figure 4.6. UV-Vis spectrum of SiC with and without epitaxial graphene.

CHAPTER 5

GRAPHENE/SEMICONDUCTOR/GRAPHENE PHOTODETECTOR MEASUREMENTS

5.1. Device Fabrication and Measurement Setup

Figure 5.1.a schematically shows the optical lithography and reactive ion etching (RIE) processes that shape the as-grown single layer epitaxial graphene into integrated finger electrodes on the underlying 4H-SiC substrate. Our device which is designed to have 25 μm wide and 100 μm long graphene finger electrodes that are laterally separated by 25 μm wide SiC spacing, can be seen under optical microscope as presented in figure 5.1.b. The fabricated device consists two sets of individual electrodes with 20 fingers.

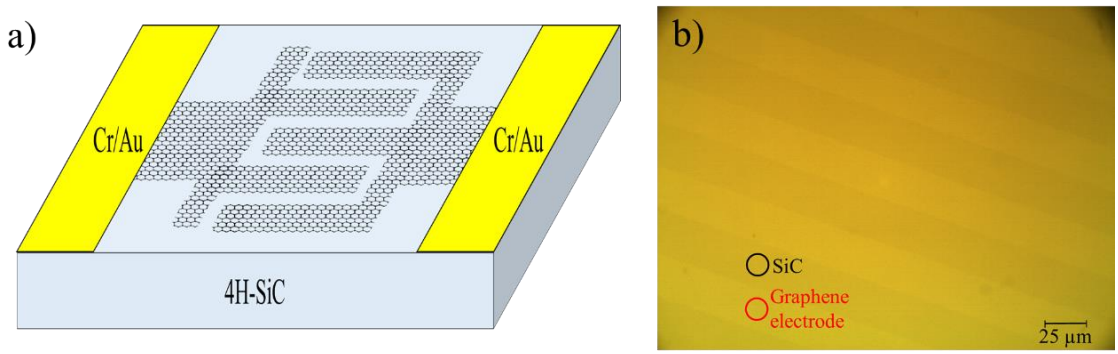

Figure 5.1. (a) The schematic illustration of the GSG device with integrated monolayer epitaxial graphene contact fingers. (b) Optical microscopy image of fabricated GSG device electrodes.

Fabrication process done in two individual steps. Firstly; finger electrodes are patterned by Micro Chemicals Az5214 negative optical lithography process, then graphene is etched by reactive O_2 gas via Oxford Plasmalab system 100 ICP 300 Deep RIE. After the fabrication of the electrodes, second optical lithography process applied to pattern electrode pads on the both side graphene electrodes to make electronic measurements possible. Cr/Au having thickness 10 nm/150 nm are deposited by Torr e-

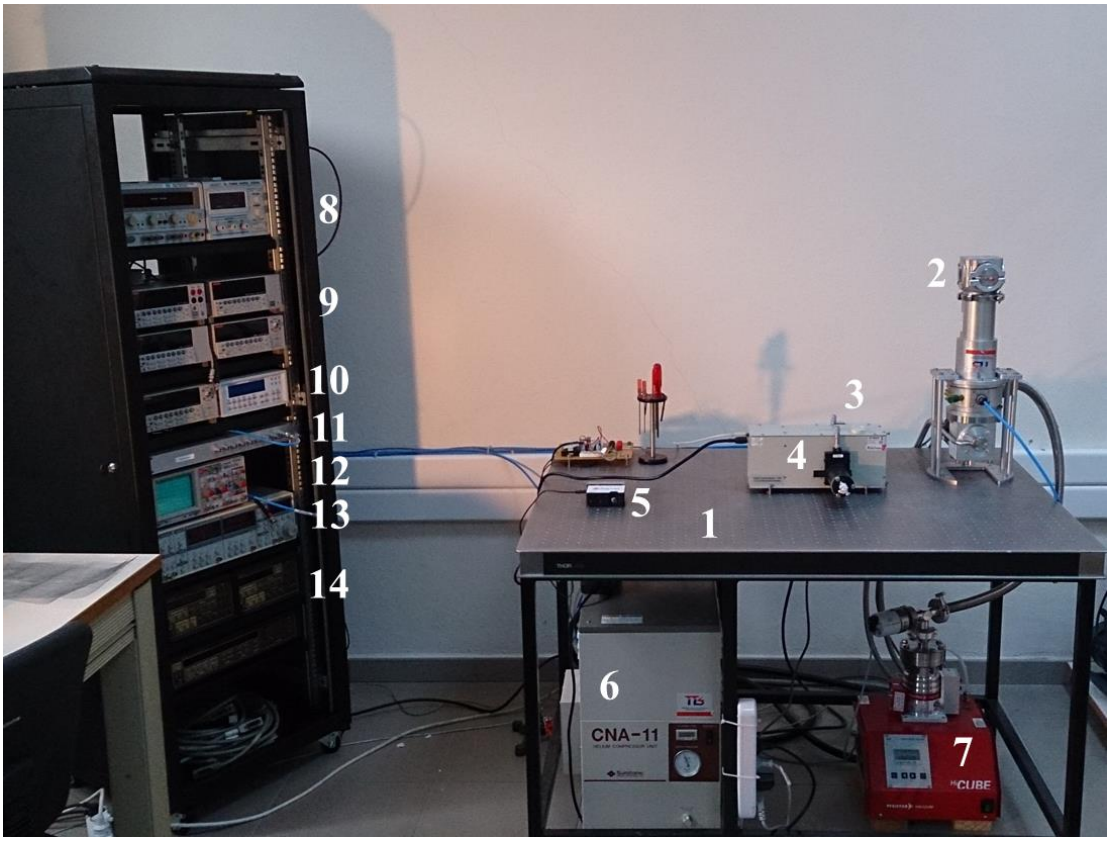

Figure 5.2. Measurement setup (1) Optic table, (2) 4.2 K cryostat (3) 300 W Halogen lamp (4) Oriel Cornerstone 130 monocromator (5) Ocean optics flame UV-Vis spectrometer, (6) Helium compressor unit, (7) Peiffer Hi-cube combination pump (Turbo molecular pump + Diaphragm pump), (8) DC power supplies, (9) Keithley 2400 source meter, Keithley 6485 picoammeter, Keithley 6220 precision current source, Keithley 2182a nanovoltmeter, (10) Lakeshore 331 temperature controller, (11) Electrical connection panel, (12) Analog oscilloscope, (13) Standford Research 830 Lock-in amplifier, (14) Keithley source measure units.

beam and thermal evaporator following the second lithography process. All device fabrication processes done in clean room facilities of Sabancı University Nanotechnology Research and Application Center (SUNUM).

Different low pressure mercury UV lamps with wavelengths of 254 nm, 311 nm and 365 nm are used for the photo-responsivity characterizations of the device. An electronic shutter mechanism is coupled to those UV sources to conduct time-resolved dark current and photocurrent measurements. Keithley 2400 source-measure unit as a voltage source and Keithley 6485 picoammeter are used to detect low level dark current and photocurrent with fA precision for the optoelectronic characterization of our device. All the optoelectronic measurements of the device were carried out ambient conditions. The measurement setup facility can be shown in figure 5.2.

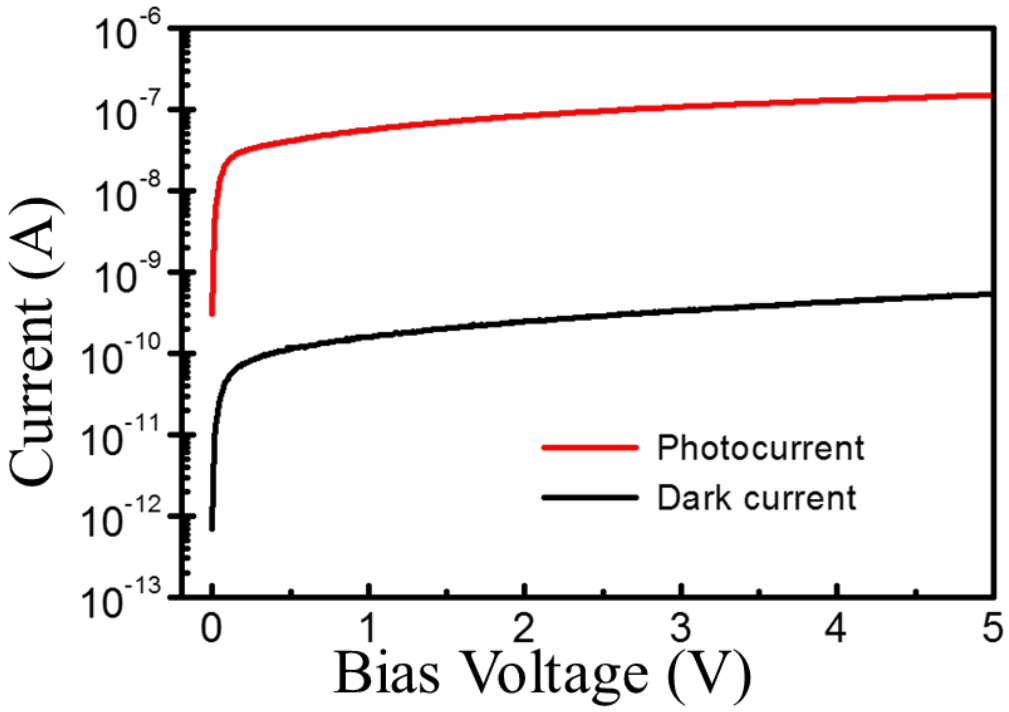

Figure 5.3. Dark current and photocurrent as a function of bias voltage measured at room temperature for the epitaxial graphene/4H-SiC GSG photodetector.

5.2. Measurements and Results

The dark current (I_d) and the photocurrent (I_p) of the sample were measured as a function of applied bias voltage (V_b) swept between 0-5 V (figure 5.2.a) to characterize the performance of the fabricated GSG device with epitaxial graphene contact electrodes both in the absence and in the presence of a 254 nm wavelength.

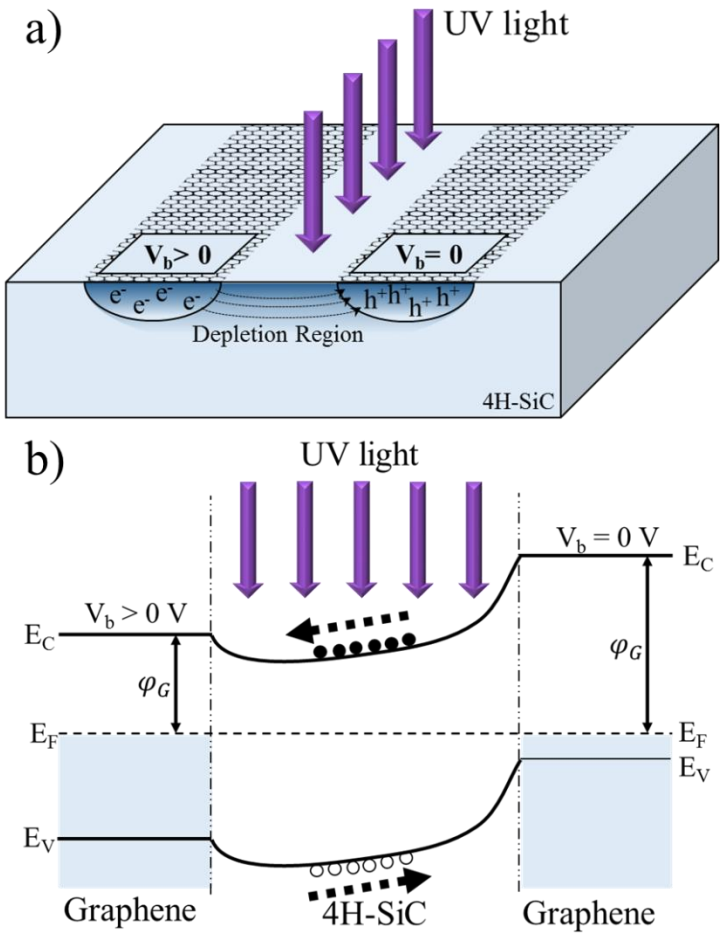

Figure 5.4. (a) The schematic cross-sectional side view of the biased GSG device with two adjacent epitaxial graphene electrodes under illumination of UV light. (b) The energy band diagram of the GSG device depicting the bias voltage induced band bending and the Schottky barrier at the epitaxial graphene/4H-SiC heterojunction.

As seen in figure 5.3, for very small bias voltages (e.g. $V_b < 0.25$ V) the well-established thermionic emission model agrees well with the increase observed in the current as mentioned in previous chapter.

The linearity of the logarithmic plot of the current in the forward bias range assures that the charge transport across the Schottky barrier is dominated as seen in figure 5.4.b. At high voltages ($V_b > 0.25$ V) the deviation from the linearity is observed due to the series resistance contributions from the underlying SiC substrate and as well due to the charge accumulation relate lowering of the Schottky barrier at graphene/SiC interface.

The schematic cross-sectional side view of the based GSG device and the corresponding energy band diagram are shown in figure 5.4.a. As the UV light is illuminated on the surface, the phonons penetrate into the surface both through the uncovered SiC and the transparent graphene electrodes in between. Electron-hole pairs are created when the UV light photons absorbed by SiC, in and below the depletion region. The applied bias voltage across graphene electrodes causes one set of electrodes to act as cathode, whence the other act as anode. The electrons are swept towards the positively biased ($V_b > 0$ V) graphene electrode where the holes are swept to the negatively biased or grounded ($V_b = 0$ V) electrode due to the effective electric field formed in the depletion region. Low resistance graphene electrodes collected the charge carriers and the corresponding photo-induced current is measured throughout the electrodes. In conventional MSM device structures due to having relatively low diffusion speed of holes, the photocurrent is limited by the reverse biased electrode, thus the current saturates. Figure 5.3 shows us that in our device the current does not completely saturate at high voltages, but keeps on rising up along the increasing voltage. Charge accumulation at the graphene/SiC interface, as seen in figure 5.4.b, results in lowering of the Schottky barrier (φ_G), which can be the reason for the slow increase in the photocurrent at higher voltages. Due to the substantial lowering of the Schottky barrier at high voltages, the dark current of our GSG device, that is in other words the leakage current, increases.

The dark I-V characteristics of the GSG structure in the bias range -2.5 V and 2.5 V displays the typical characteristics expected for two back-to-back Schottky diodes, as seen on figure 5.5.a. The asymmetry of the dark I-V curves observed for all measurements suggests that the Schottky junctions formed at different graphene fingers are not uniform. The defect driven variations in the Schottky barrier height at the interface between epitaxial graphene/4H-SiC heterojunction [68] might be responsible for the asymmetric structure of the dark I-V curve.

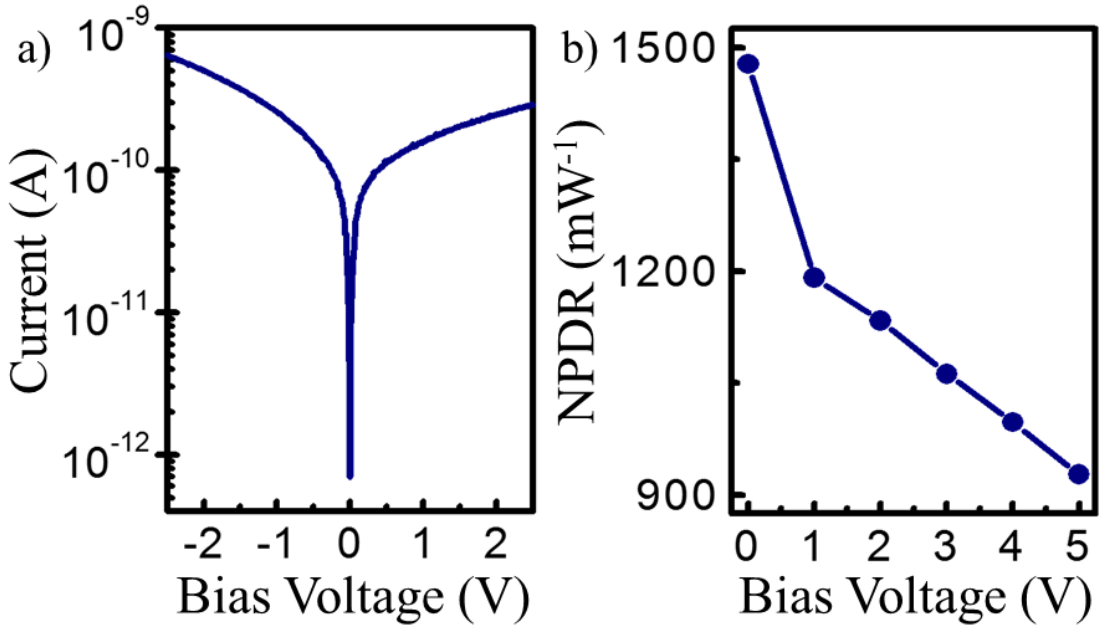

Figure 5.5. (a) The dark I-V characteristics of the epitaxial graphene/SiC GSG device illustrated in figure 5.1. (b) The measured NPDR parameter of the device as a function of bias voltage.

In the absence of the illumination the dark current of the device for a bias voltage of 0 V was measured as 0.7 pA, which is three orders of magnitude smaller than the photocurrent of the device. The normalized photo-to-dark current ratio NPDR= $(I_p/I_d)/P_i$ metric of our sample, that provided a direct information about the responsivity of our photodetector and the noise equivalent power though the dark current as well [73], was determined as an assessment of the device performance. In our case, for an incident optical power of P_i = 0.3 mW, the NPDR versus forward bias voltage was displayed in figure 5.5.b. As the bias voltage increased from 0 V to 5 V the NPDR value of our sample decreased from ~$15x10^2$ mW^{-1} down to ~$9x10^2$ mW^{-1}. The main reason of the increase is the rise in the dark current at high bias voltages, that climbs up to 0.1 nA at 5 V. It is important to note that the obtained NPDR values of our device is lower than those reported for 4H-SiC based MSM photodetectors with low leakage currents [72].

Under 254 nm light illumination, the time resolved photocurrent characteristics of the GSG device was investigated over several turning switching on/off cycles at

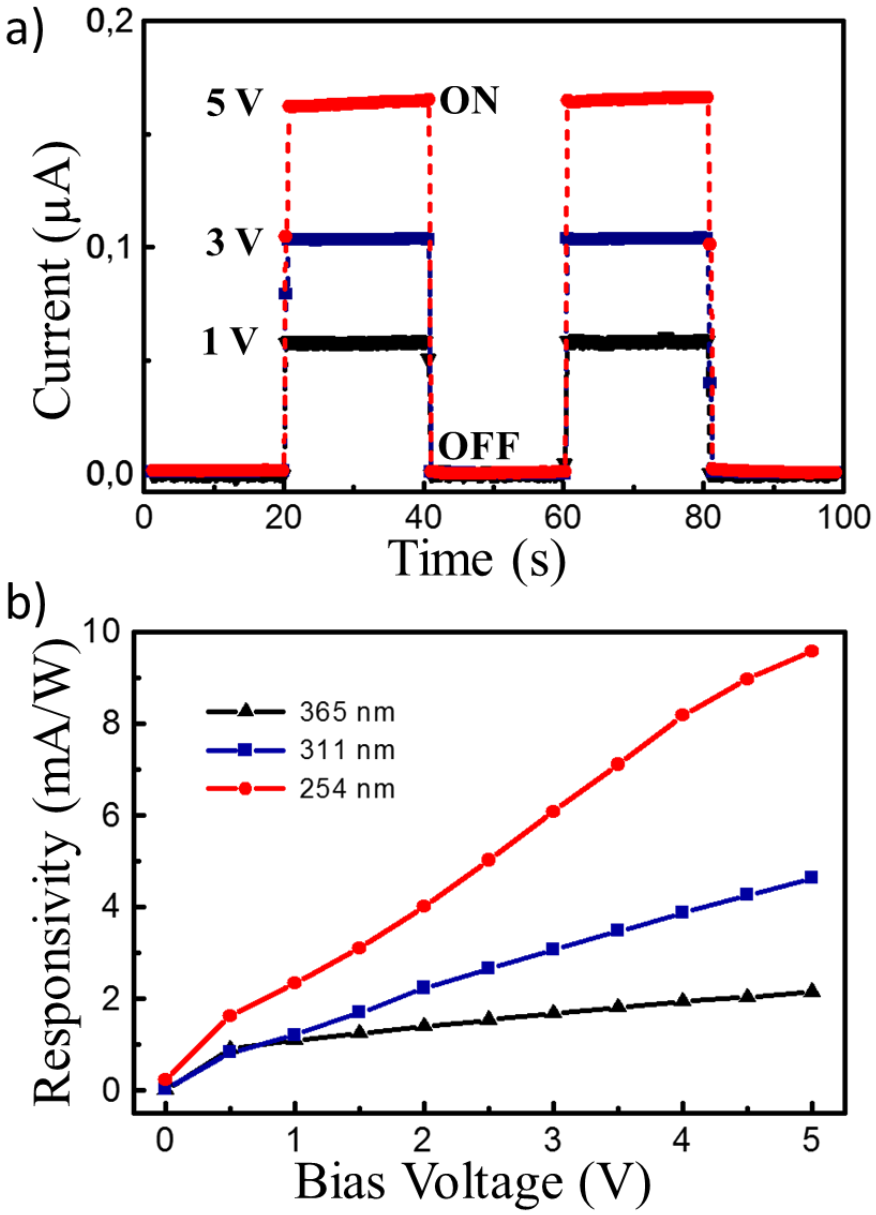

Figure 5.6. (a) Time response characteristics of the GSG device under 254 nm UV light illumination demonstrating that the fast photoresponse is retained at different bias voltages. (b) Wavelength dependent photo responsivity of the device as a function of bias voltage.

different bias voltages. The measurements were taken for a time interval of 0-100 s where both turn-on time and turn-off time were set to 20 s. The measured current of the device exhibited two distinct states given as 0.1 nA in dark and an average photocurrent of 0.1 μA under light illumination for on and off states of the UV light irradiation (figure 5.6.a). The uniform and stable profile of the time-resolved photocurrent plots confirms that the device had an excellent photocurrent reversibility and stability. Additionally the steep increase of the current from one state to other indicates a fast response speed for the device. The high speed response of the device, similar to the case given in reference [74], can be related to the built-in local electric fields at the graphene/SiC interface arising from the charge transfer doping driven bond-polarization effect [75].

The sample responsivity measurements as a function of the applied bias for three different UV wavelengths with same illumination power concludes that the responsivity under 254 nm wavelength UV light shows a linear dependence for applied bias, as typical for an MSM type photodetector as shown in figure 5.6.b. It is observed that the decrease in the illumination wavelength leads to an increase in the responsivity and thus the integral gain. The device shows a smaller photocurrent-to-darkcurrent contrast ratio $\left(\frac{I_p}{I_d}\right)$ for larger wavelengths when compared to the illumination under 254 nm light. The underlying phenomenon is the very small (> 1%) quantum efficiency of the internal photoemission for 311 and 364 nm wavelengths. The responsivity converges to a saturation level of 4.2 $mA.W^{-1}$ and 2.0 $mA.W^{-1}$ for 311 nm and 365 nm wavelengths respectively as the applied voltage approaches to 5 V. The peak responsivity is defined as;

$$R_\lambda = \left(\frac{I_\lambda}{P_\lambda S}\right) \tag{5.1}$$

the wavelength dependent photocurrent $\left(I_\lambda = I_p - I_d\right)$ generated per unit power (P_λ) upon incident light on the effective surface area (S) of the detector. Owing to finite charge carrier lifetime and the fact that only a fraction of the electrons with high enough kinetic energy to overcome the Schottky barrier are collected at the electrodes, the observed photocurrent increases linearly with the bias voltage. The saturation of photocurrent at higher bias voltages indicates that all the photo-generated charge carriers are already collected at the electrode. It is important to note that the average voltage dependent UV

photo-responsivity of our sample is one order of magnitude larger than those reported for GaN based MSM type detectors with CVD grown multilayer graphene Schottky electrodes [19]. The fact that the optoelectronic properties of graphene can be tailored by fluorescent biomolecules and colloidal quantum dots [76], gives graphene an advantage over conventional transparent conductive electrodes. Graphene electrodes in conjunction with such light-harvesting nanostructures can be utilized as individual photo-active components which also contribute to the photosensitivity of our GSG device.

CHAPTER 6

THE EFFECT OF QDOTS ON THE PHOTORESPONSIVITY OF GSG DEVICE

6.1. Introduction

The main drawback of using graphene as transparent conductive electrode in optoelectronic and photovoltaic devices is the low gain characteristics, thus many researches have focused on increasing the gain by placing fluorescent molecules and quantum dots (QDs) on the graphene matrix [77]. Addition of such nanostructures has been shown to enhance the photocurrents of the respective device via the optical excitation of those nanostructures which results in a resonant charge transfer between the nanostructures and graphene. QDs are mostly preferred due to their inertness, size-dependent tuneable optical properties, unique compatibility to form heterostructures, and strong light harvesting capabilities. The photo-excited QDs produce electron-hole pairs that change the conductance of graphene layer and thus result in altered device characteristics [78].

6.2. Device Fabrication and Measurement Setup

In this work, same fabrication methods and parameters which mentioned in previous chapters are used to pattern GSG device. The QDs were synthesized in aqueous solution by using the method described in ref [79] and were drop-casted directly on the interdigitated surface of the GSG sample. Figure 6.1 illustrates the schematics of our fabricated graphene-semiconductor-graphene (GSG) device after the deposition of CdTe/CdS (core/shell) QDs with an average diameter of about 5.3 nm. The optoelectronic characterizations of the sample were done with 365 nm wavelength UV light illumination before and after the deposition of QD thin film with two different thicknesses (e.g., t = 60 nm and t = 120 nm). The wavelength of the UV light exposed to the sample surface is sufficient enough to create excitons in the QD film with more than

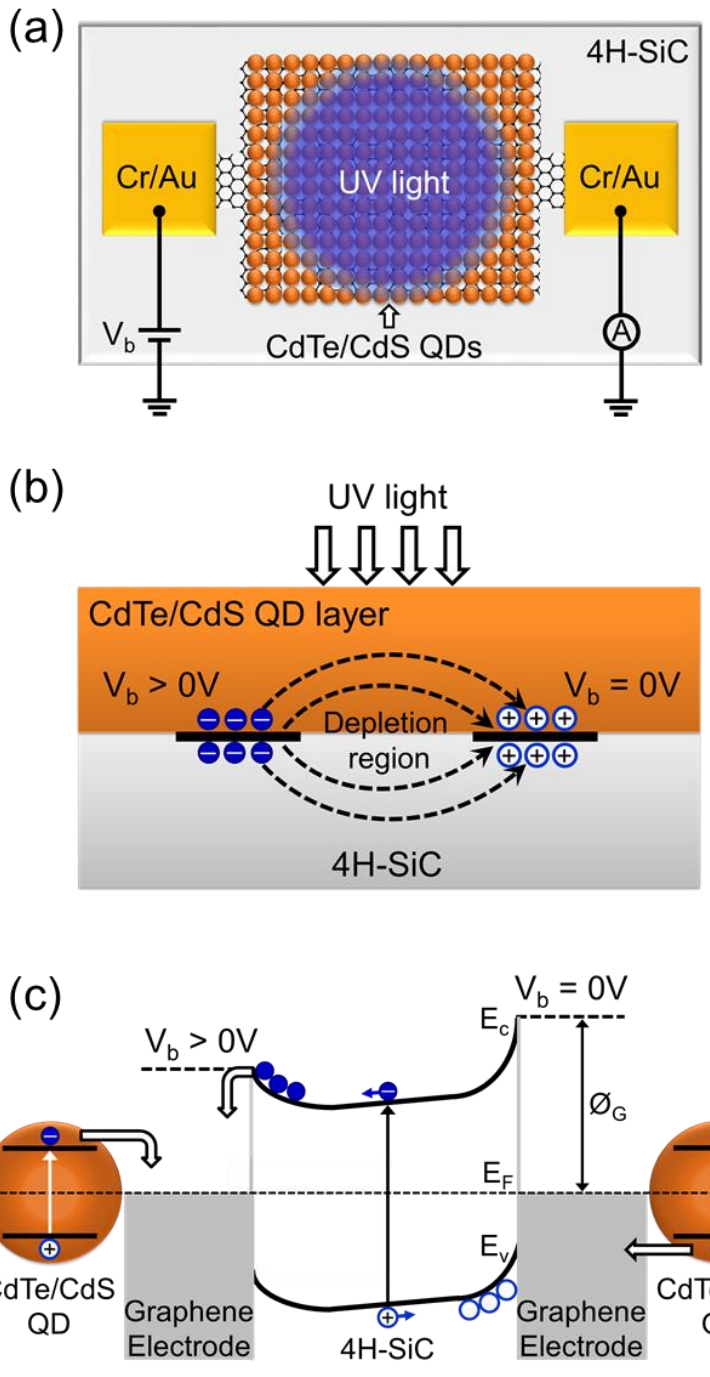

Figure 6.1. (a) Schematic illustration of the GSG device with drop-casted QDs on top of the device. (b) The schematic cross-sectional side view of the biased GSG device with drop-casted QDs. The dashed and curved arrows depict the electric field lines in the depletion region underneath the SiC surface and QD layer. (c) The energy band diagram of the QD/Graphene/SiC heterostructure depicting the bias voltage induced band bending and the Schottky barrier at the graphene/4H-SiC junction.

45% quantum yield and also corresponds well to the optical absorption edge of 4H-SiC due to its 3.2 eV energy band gap.

6.3. Measurements and Results

In figure 6.2 the photocurrent (I_p) and dark current (I_d) characteristics of the sample are compared before and after the deposition of QD layer. Both I_p and I_d of the sample are recorded as a function of applied bias voltage (V_b) which is swept between 0 and 5 V. Compared to the bare GSG sample the presence of QD film on top causes a substantial increase in the measured I_p. It should be noted that the increment of I_p is proportional to the layer thickness. In all the experiments the I_p of the sample increases linearly at low voltage ranges (e.g., $V_b < 0.5$ V) in accordance with the well-established thermionic-emission model. The detailed information about thermionic-emission model is described in previous chapters. The deviation from linearity observed at high voltages (e.g., $V_b >$ 0.5 V) can be attributed to the series resistance contributions from both the underlying SiC substrate and QD layer and as well as to the charge accumulation induced lowering of the Schottky barrier at the QD/graphene/SiC interface. Figure 6.2.b shows the dark I-V characteristics of the GSG device with and without the QD layer. Charge accumulation induced reduction of the Schottky barrier height due to the QD layer also increases the I_d level of the device. For the bare GSG sample, the dark current is dominated by the thermionic emission current of the charge carriers from the underlying SiC substrate, and thus the magnitude of the dark current is determined only by the Schottky barrier height at the graphene/SiC interface. It is most likely that the inserted thin QD layer has suppressed the effective Schottky barrier height of the pristine device. Besides, the increment of the dark current can also be related to a possible shunt conduction path provided by the QD layer itself.

The photocurrent generation mechanism in the QD/GSG tandem structure is illustrated with the schematic in figure 6.1. When the UV light impinges on the device surface, the photons first penetrate into the QD layer and reach the underlying SiC substrate both in through the transparent graphene electrodes and SiC regions in between these electrodes. The optical absorption measurements conducted for 365 nm UV light inferred that the absorption level of 60 nm thick QD layer is about 15% whereas it increases to 52% for 120 nm thick QD layer. Upon the absorption of UV

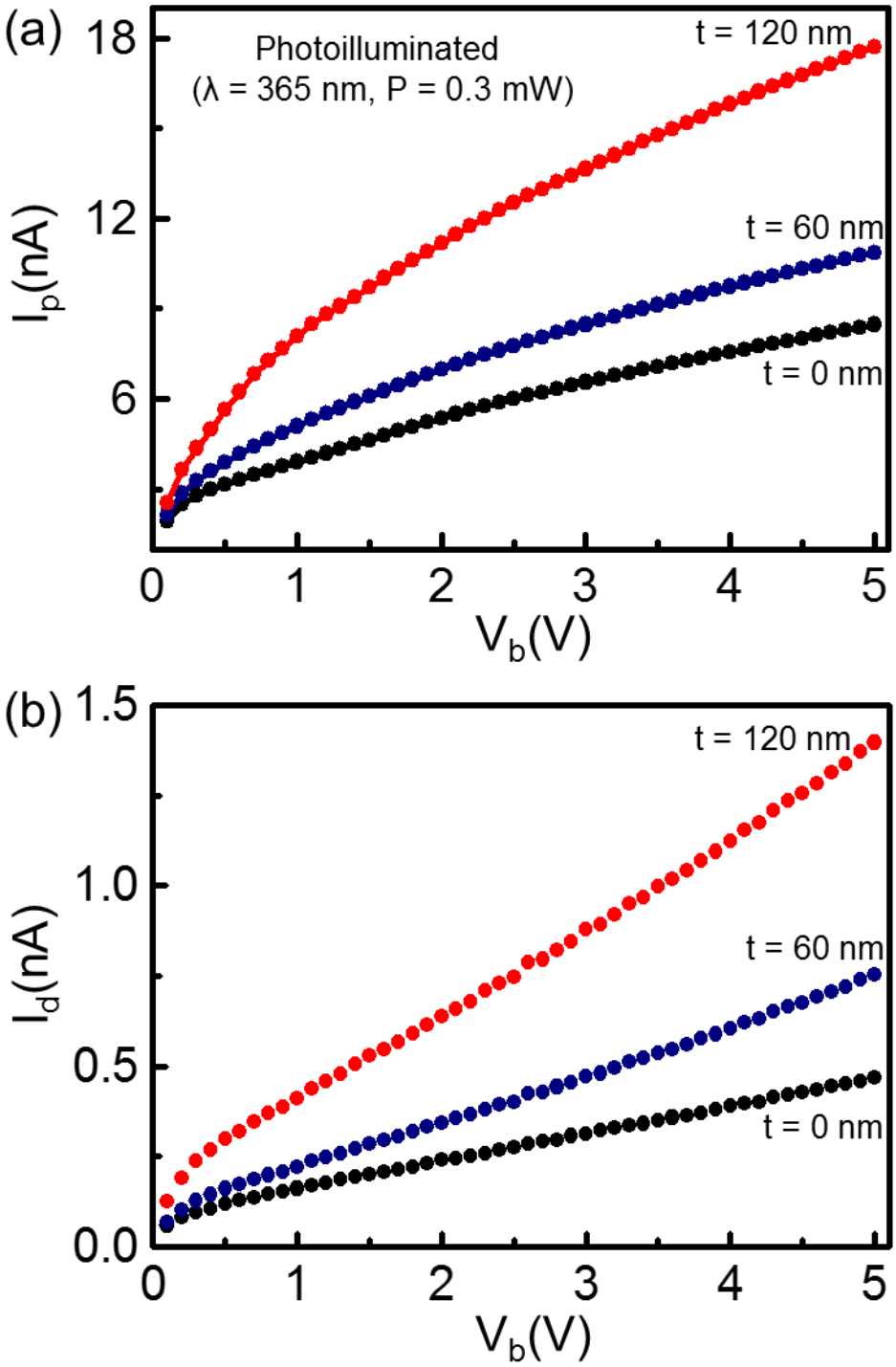

Figure 6.2. (a) and (b) illustrates photocurrent and dark current as a function of bias voltage measured at room temperature for the photodetector with different QD film thickness. The photocurrent measured under 365 nm UV illumination.

photons by QD layer and SiC substrate electron-hole pairs are created simultaneously at the depletion region. If a bias voltage is applied across the graphene electrodes, then one set of the electrodes acts as cathode and the other as anode. As displayed in figure 6.1.b the effective electric field in the depletion region sweeps the photo-generated electrons towards the positively biased graphene electrode ($V_b > 0$ V), while the holes drift towards the opposite electrode which is reverse biased or grounded ($V_b = 0$ V). The photo-induced charge carriers created both in the QD layer and in the SiC substrate are collected by conductive graphene electrodes and the corresponding I_p is measured via these electrodes. In a typical MSM type device structure, the reverse biased electrode usually limits I_p and results in a current saturation due to low diffusion speed of holes. However, figure 6.2 shows that after the first step rise, the current does not completely saturate at high voltages but slightly rise up with increasing V_b. The observed voltage dependent increase of I_p is typical and can be associated with the lowering of the Schottky barrier due to charge accumulation at the QD/graphene/SiC interface as depicted in figure 6.1.b. The enhanced I_p is ascribed to electron excitation from the valence band to the conduction band of CdTe/CdS QDs and simultaneously to the electric field driven injection of the photoexcited charge carriers to the respective graphene electrodes as shown in the schematic illustration of the energy band diagram (figure 6.1.c). The supplementation of the QDs on the fabricated device gives rise to the band alignment between the two materials, resulting in the allowance of photo-induced electron transfer from the QDs to graphene. Additionally, the inserted QD layer is thought to provide large surface areas and short diffusion lengths for the photo-generated charge carriers [80].

As an objective assessment for the change in the device performance due to the QD layer, we evaluated the photocurrent enhancement factor $PCEF = [\Delta I^w / \Delta I^{wo}]$ of the sample. Here $\Delta I^w = (I_p^w - I_d^w)$ and $\Delta I^{wo} = \left(I_p^{wo} - I_d^{wo}\right)$ correspond to the net photocurrents of the device with and without the QD layer, respectively. Figure 6.3.a shows the change in the PCEF of our device for 60 nm and 120 nm CdTe/CdS QD film thicknesses as a function of applied V_b. The graph reveals two distinct characteristics for the applied voltage ranges below and above 1 V. For the applied voltages up to 1 V the PCEF increases almost linearly due to the photo-generated charge carriers harvested both from the QD layer and SiC substrate. Compared to the device with 60 nm thick QD layer the PCEF of the one with 120 nm thick QD layer is strongly enhanced due to the

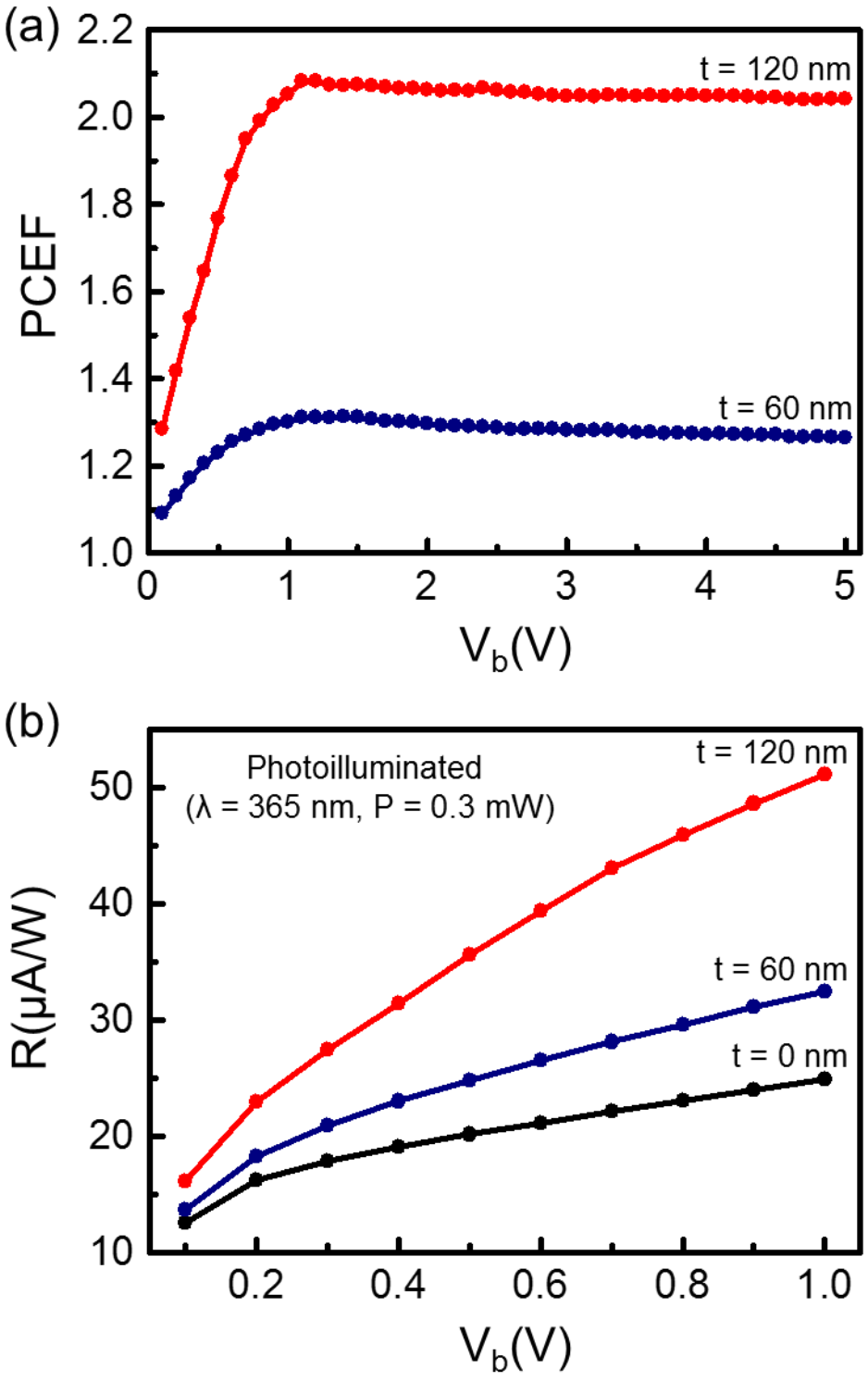

Figure 6.3. (a) QD film thickness dependent PCEF of device as a function of bias voltage. (b) QD film thickness dependent photo-responsivity (R) of the device as a function of bias voltage.

higher QD density. The observed linearity of PCEF for the voltage ranges below 1 V is related to the rectifying character of the Schottky barrier present at the QD/graphene/SiC interface. In addition; for both QD thicknesses the initial linear increase at the PCEF can be also explained in terms of the intensifying electrical field formed between the two graphene electrodes as the density of the QD increases. Similar effect has also been reported for gold nanoparticles decorated with PbS QDs [81]. The observed slight and gradual decrease in the PCEF of the device above 1 V is due to the abrupt increase in the dark current. At high voltages the Schottky barrier is strongly suppressed so that the device already reaches to the flat band condition. This would strongly dominate the dark current of the device. The applied voltage (1 V) which brings the device to the flat band level corresponds to the height of the Schottky barrier (~1 eV) at the graphene/SiC interface. At high voltages the dark current increases linearly while photocurrent converges to a saturation thus supressing slightly the PCEF.

The responsivity of the sample is measured as a function of the applied bias for two different QD layer thickness and the obtained results are compared with the responsivity of the sample without the QD layer. The calculation of responsivity is discussed in previous chapter. For a wavelength of 365 nm and of P = 0.3 mW illumination power, the corresponding photocurrent increases with the bias voltage, which is due to the finite carrier life-time and only a part of the photo-generated charge carriers, with large enough kinetic energies to overcome the Schottky barrier, are collected at one of the graphene electrodes. The responsivity of the GSG device was also found to be strongly influenced by the amount of QDs. As shown in figure 6.3.b, the shift of the responsivity transfer curve increases with the increase of QD layer thickness under the same light irradiation (P = 0.3 mW). Since the carrier mobility of graphene is more than four orders of magnitude higher than the mobility of QD film, the observed responsivity enhancement in the device is reasonable.

CHAPTER 7

CONCLUSIONS

In this thesis work, a UV sensitive GSG photodetector based on the Schottky junction at the epitaxial graphene/SiC interface is fabricated and characterized. One atom thick epitaxial graphene grown on SI 4H-SiC substrate is interdigitated by a single step lithography process to collect UV light induced photo-generated charge carriers generated in the semi-conductive substrate. The I-V characteristics demonstrated a rectifying behavior of the heterojunction that manifests the existence of Schottky barrier at the epitaxial graphene/SiC interface. An abrupt response even at 0 V applied bias is observed for the fabricated device with transparent epitaxial graphene electrodes. Yet due to the enhancement of the dark current at high voltages, the NPDR value of the sample is found to decrease about 40% as the applied voltage increased from 0 to 5 V. It is proven by obtained data from the light on/off characteristics that epitaxial graphene/SiC heterojunction is suitable for UV photo-detection with fast response speed. The sample is found to have a higher responsivity under an irradiation wavelength of 254 nm when compared to the illumination under 311 and 365 nm. The early saturated maximum responsivity of the GSG samples with graphene electrodes shows that the fabricated device is suitable to be implemented as UV sensor systems operating at relatively low voltages. We believe that the obtained results will provide an insight for the future adaptation of epitaxial graphene as a transparent and conductive electrode especially for the existing SiC based optoelectronic device applications.

We also showed that the responsivity of the GSG photodetector can be enhanced by colloidal QDs. The I-V measurements showed additional contribution of QDs to the photocurrent of our fabricated device. We observed that for $V_b > 1$ V, PCEF can be enhanced by 2 times for when GSG device coated with 120 nm QDs. We found that the dark current of the device is increased due to the suppression of the rectifying Schottky barrier height. It is also showed that, especially at low voltage ranges ($V_b < 1$ V), the photo-responsivity level of the bare device is increased about 2 times by drop-casting a thin layer of QD film on the sample surface. The obtained experimental results imply that the gain of the GSG device can be further increased simply by addition of colloidal QDs.

REFERENCES

[1] X. Lu, M. Yu, H. Huang, and R. S. Ruoff, “Tailoring graphite with the goal of achieving single sheets,” *Nanotechnology*, vol. 10, no. 3, p. 269, 1999.

[2] L. D. Landau, “Zur Theorie der phasenumwandlungen II,” *Phys. Z. Sowjetunion*, vol. 11, pp. 26–35, 1937.

[3] J. Stangl, V. Hol\`y, and G. Bauer, “Structural properties of self-organized semiconductor nanostructures,” *Rev. Mod. Phys.*, vol. 76, no. 3, p. 725, 2004.

[4] J. C. Meyer, A. K. Geim, M. I. Katsnelson, K. S. Novoselov, T. J. Booth, and S. Roth, “The structure of suspended graphene sheets,” *Nature*, vol. 446, no. 7131, pp. 60–63, 2007.

[5] K. S. Novoselov, D. Jiang, F. Schedin, T. J. Booth, V. V Khotkevich, S. V Morozov, and A. K. Geim, “Two-dimensional atomic crystals,” *Proc. Natl. Acad. Sci. U. S. A.*, vol. 102, no. 30, pp. 10451–10453, 2005.

[6] A. Geim and K. Novoselov, “The rise of graphene,” *Nat. Mater.*, pp. 183–192, 2007.

[7] M. I. Katsnelson, “Graphene: carbon in two dimensions,” *Mater. today*, vol. 10, no. 1, pp. 20–27, 2007.

[8] K. S. Novoselov, A. K. Geim, S. V Morozov, D. Jiang, Y. Zhang, S. V Dubonos, I. V and Grigorieva, and A. A. Firsov, “Electric field effect in atomically thin carbon films,” *Science (80-.).*, vol. 306, no. 5696, pp. 666–669, 2004.

[9] K. S. Novoselov, E. McCann, S. V Morozov, V. I. Fal’ko, M. I. Katsnelson, U. Zeitler, D. Jiang, F. Schedin, and A. K. Geim, “Unconventional quantum Hall effect and Berry’s phase of 2π in bilayer graphene,” *Nat. Phys.*, vol. 2, no. 3, pp. 177–180, 2006.

[10] C. Yan\ik and I. I. Kaya, “Local breakdown of the quantum Hall effect in narrow single layer graphene Hall devices,” *Solid State Commun.*, vol. 160, pp. 47–51, 2013.

[11] K. S. A. Novoselov, A. K. Geim, Sv. Morozov, D. Jiang, Mi. Katsnelson, Iv. Grigorieva, Sv. Dubonos, and Aa. Firsov, “Two-dimensional gas of massless Dirac fermions in graphene,” *Nature*, vol. 438, no. 7065, pp. 197–200, 2005.

[12] F. Schedin, A. K. Geim, S. V Morozov, E. W. Hill, P. Blake, M. I. Katsnelson, and K. S. Novoselov, “Detection of individual gas molecules adsorbed on graphene,” *Nat. Mater.*, vol. 6, no. 9, pp. 652–655, 2007.

[13] C. K. Wang, S.-J. Chang, Y.-K. Su, Y.-Z. Chiou, S. C. Chen, C. S. Chang, T. K. Lin, H. L. Liu, and J. J. Tang, "GaN MSM UV photodetectors with titanium tungsten transparent electrodes," *Electron Devices, IEEE Trans.*, vol. 53, no. 1, pp. 38–42, 2006.

[14] Y.-K. Su, Y.-Z. Chiou, C.-S. Chang, S.-J. Chang, Y.-C. Lin, and J. F. Chen, "4H-SiC metal--semiconductor--metal ultraviolet photodetectors with Ni/ITO electrodes," *Solid. State. Electron.*, vol. 46, no. 12, pp. 2237–2240, 2002.

[15] A. Sciuto, F. Roccaforte, S. Di Franco, S. F. Liotta, G. Bonanno, and V. Raineri, "High efficiency 4H-SiC Schottky UV-photodiodes using self-aligned semitransparent contacts," *Superlattices Microstruct.*, vol. 41, no. 1, pp. 29–35, 2007.

[16] Y. G. Zhang, A. Z. Li, and A. G. Milnes, "Metal-semiconductor-metal ultraviolet photodetectors using 6H-SiC," *Photonics Technol. Lett. IEEE*, vol. 9, no. 3, pp. 363–364, 1997.

[17] S. P. S.-J. P. S. J. Chang, T. K. K. Lin, Y.-K. Y. K. Su, Y. Z. Z. Chiou, C. K. K. Wang, S. P. S.-J. P. S. J. Chang, C. M. M. Chang, J. J. J. Tang, and B. R. R. Huang, "Homoepitaxial ZnSe MSM photodetectors with various transparent electrodes," *Mater. Sci. Eng. B*, vol. 127, no. 2–3, pp. 164–168, Feb. 2006.

[18] T. H. Seo, K. J. Lee, A. H. Park, C.-H. Hong, E.-K. Suh, S. J. Chae, Y. H. Lee, T. V. Cuong, V. H. Pham, J. S. Chung, E. J. Kim, S.-R. Jeon, and others, "Enhanced light output power of near UV light emitting diodes with graphene/indium tin oxide nanodot nodes for transparent and current spreading electrode," *Opt. Express*, vol. 19, no. 23, pp. 23111–7, Nov. 2011.

[19] C. J. Lee, H. G. Cha, S. K. Hong, S. H. Doh, Y. S. Koo, B. J. Cho, and S. H. Hahm, "GaN MSM UV Sensor Using Multi-Layer Graphene Schottky Electrodes," in *Applied Mechanics and Materials*, 2014, vol. 481, pp. 146–149.

[20] C. Celebi, C. Yanik, A. G. Demirkol, and I. I. Kaya, "The effect of a SIC cap on the growth of epitaxial graphene on SIC in ultra high vacuum," *Carbon N. Y.*, vol. 50, no. 8, pp. 3026–3031, 2012.

[21] C. Çelebi, C. Yanik, A. G. Demirkol, and I. I. Kaya, "Control of the graphene growth rate on capped SiC surface under strong Si confinement," *Appl. Surf. Sci.*, vol. 264, pp. 56–60, 2013.

[22] W. A. De Heer, C. Berger, X. Wu, M. Sprinkle, Y. Hu, M. Ruan, J. A. Stroscio, P. N. First, R. Haddon, B. Piot, and others, "Epitaxial graphene electronic structure and transport," *J. Phys. D. Appl. Phys.*, vol. 43, no. 37, p. 374007, 2010.

[23] P. W. Sutter, J.-I. Flege, and E. A. Sutter, "Epitaxial graphene on ruthenium," *Nat. Mater.*, vol. 7, no. 5, pp. 406–411, 2008.

[24] G. Eda, G. Fanchini, and M. Chhowalla, “Large-area ultrathin films of reduced graphene oxide as a transparent and flexible electronic material,” *Nat. Nanotechnol.*, vol. 3, no. 5, pp. 270–274, 2008.

[25] K. S. Kim, Y. Zhao, H. Jang, S. Y. Lee, J. M. Kim, K. S. Kim, J.-H. Ahn, P. Kim, J.-Y. Choi, and B. H. Hong, “Large-scale pattern growth of graphene films for stretchable transparent electrodes,” *Nature*, vol. 457, no. 7230, pp. 706–710, 2009.

[26] B. Obradovic, R. Kotlyar, F. Heinz, P. Matagne, T. Rakshit, M. D. Giles, M. A. Stettler, and D. E. Nikonov, “Analysis of graphene nanoribbons as a channel material for field-effect transistors,” *Appl. Phys. Lett.*, vol. 88, no. 14, p. 142102, 2006.

[27] A. K. Geim, “Graphene: status and prospects,” *Science (80-.).*, vol. 324, no. 5934, pp. 1530–1534, 2009.

[28] C. Attaccalite, A. Grüeneis, T. Pichler, and A. Rubio, “Ab-initio band structure of doped graphene,” *arXiv Prepr. arXiv0808.0786*, 2008.

[29] S. Reich, J. Maultzsch, C. Thomsen, and P. Ordejon, “Tight-binding description of graphene,” *Phys. Rev. B*, vol. 66, no. 3, p. 35412, 2002.

[30] J. Güttinger, F. Molitor, C. Stampfer, S. Schnez, A. Jacobsen, S. Dröscher, T. Ihn, and K. Ensslin, “Transport through graphene quantum dots,” *Reports Prog. Phys.*, vol. 75, no. 12, p. 126502, 2012.

[31] J.-H. Chen, C. Jang, S. Xiao, M. Ishigami, and M. S. Fuhrer, “Intrinsic and extrinsic performance limits of graphene devices on SiO2,” *Nat. Nanotechnol.*, vol. 3, no. 4, pp. 206–209, 2008.

[32] A. Akturk and N. Goldsman, “Electron transport and full-band electron-phonon interactions in graphene,” *J. Appl. Phys.*, vol. 103, no. 5, p. 53702, 2008.

[33] K. I. Bolotin, K. J. Sikes, Z. Jiang, M. Klima, G. Fudenberg, J. Hone, P. Kim, and H. L. Stormer, “Ultrahigh electron mobility in suspended graphene,” *Solid State Commun.*, vol. 146, no. 9, pp. 351–355, 2008.

[34] N. Tombros, A. Veligura, J. Junesch, J. J. van den Berg, P. J. Zomer, M. Wojtaszek, I. J. V. Marun, H. T. Jonkman, and B. J. van Wees, “Large yield production of high mobility freely suspended graphene electronic devices on a polydimethylglutarimide based organic polymer,” *J. Appl. Phys.*, vol. 109, no. 9, p. 93702, 2011.

[35] P. Norton, T. Braggins, and H. Levinstein, “Impurity and lattice scattering parameters as determined from Hall and mobility analysis in n-type silicon,” *Phys. Rev. B*, vol. 8, no. 12, p. 5632, 1973.

[36] T. Ando, Y. Zheng, and H. Suzuura, “Dynamical conductivity and zero-mode anomaly in honeycomb lattices,” *J. Phys. Soc. Japan*, vol. 71, no. 5, pp. 1318–1324, 2002.

[37] V. P. Gusynin, S. G. Sharapov, and J. P. Carbotte, “Unusual microwave response of Dirac quasiparticles in graphene,” *Phys. Rev. Lett.*, vol. 96, no. 25, p. 256802, 2006.

[38] L. A. Falkovsky and S. S. Pershoguba, “Optical far-infrared properties of a graphene monolayer and multilayer,” *Phys. Rev. B*, vol. 76, no. 15, p. 153410, 2007.

[39] A. B. Kuzmenko, E. van Heumen, F. Carbone, and D. van der Marel, “Universal dynamical conductance in graphite,” *arXiv Prepr. arXiv0712.0835*, 2007.

[40] T. Stauber, N. M. R. Peres, and A. K. Geim, “Optical conductivity of graphene in the visible region of the spectrum,” *Phys. Rev. B*, vol. 78, no. 8, p. 85432, 2008.

[41] R. R. Nair, P. Blake, A. N. Grigorenko, K. S. Novoselov, T. J. Booth, T. Stauber, N. M. R. Peres, and A. K. Geim, “Fine structure constant defines visual transparency of graphene,” *Science (80-.).*, vol. 320, no. 5881, p. 1308, 2008.

[42] J. Wu, M. Agrawal, H. A. Becerril, Z. Bao, Z. Liu, Y. Chen, and P. Peumans, “Organic light-emitting diodes on solution-processed graphene transparent electrodes,” *ACS Nano*, vol. 4, no. 1, pp. 43–48, 2009.

[43] L. Gomez De Arco, Y. Zhang, C. W. Schlenker, K. Ryu, M. E. Thompson, and C. Zhou, “Continuous, highly flexible, and transparent graphene films by chemical vapor deposition for organic photovoltaics,” *ACS Nano*, vol. 4, no. 5, pp. 2865–2873, 2010.

[44] G. Jo, M. Choe, C.-Y. Cho, J. H. Kim, W. Park, S. Lee, W.-K. Hong, T.-W. Kim, S.-J. Park, B. H. Hong, and others, “Large-scale patterned multi-layer graphene films as transparent conducting electrodes for GaN light-emitting diodes,” *Nanotechnology*, vol. 21, no. 17, p. 175201, 2010.

[45] A. der Ziel, *Solid state physical electronics*, vol. 3. Prentice-Hall Englewood Cliffs, 1968.

[46] N. F. Mott, “Note on the contact between a metal and an insulator or semi-conductor,” in *Mathematical Proceedings of the Cambridge Philosophical Society*, 1938, vol. 34, no. 04, pp. 568–572.

[47] E. H. Rhoderick and R. H. Williams, *Metal-semiconductor contacts*. Clarendon Press Oxford, 1988.

[48] S. Tongay, M. Lemaitre, X. Miao, B. Gila, B. R. Appleton, and A. F. Hebard, “Rectification at graphene-semiconductor interfaces: zero-gap semiconductor-based diodes,” *Phys. Rev. X*, vol. 2, no. 1, p. 11002, 2012.

[49] H. A. Bethe, “MIT Radiation Laboratory Report 43/12.” MIT, Cambridge, MA, 1942.

[50] S. M. Sze and K. K. Ng, *Physics of semiconductor devices*. John Wiley & Sons, 2006.

[51] M. E. Levinshtein, S. L. Rumyantsev, and M. S. Shur, *Properties of Advanced Semiconductor Materials: GaN, AIN, InN, BN, SiC, SiGe*. John Wiley & Sons, 2001.

[52] M. B. Klarskov, "Fabrication and Multiprobe ElectricalCharacterization of Nanostructures," 2012.

[53] D. B. Slater Jr, G. M. Johnson, L. A. Lipkin, A. V Suvorov, and J. W. Palmour, "Demonstration of a 6H-SiC CMOS technology," in *Device Research Conference, 1996. Digest. 54th Annual*, 1996, pp. 162–163.

[54] W. Xie, J. A. Cooper Jr, and M. R. Melloch, "Monolithic NMOS digital integrated circuits in 6H-SiC," *Electron Device Lett. IEEE*, vol. 15, no. 11, pp. 455–457, 1994.

[55] J. N. Pan, J. A. Cooper Jr, and M. R. Melloch, "Self-aligned 6H-SiC MOSFETs with improved current drive," *Electron. Lett.*, vol. 31, no. 14, pp. 1200–1201, 1995.

[56] S. T. Sheppard, M. R. Melloch, and J. A. Cooper Jr, "Experimental demonstration of a buried-channel charge-coupled device in 6H silicon carbide," *Electron Device Lett. IEEE*, vol. 17, no. 1, pp. 4–6, 1996.

[57] G. R. Fisher and P. Barnes, "Towards a unified view of polytypism in silicon carbide," *Philos. Mag. B*, vol. 61, no. 2, pp. 217–236, 1990.

[58] L. S. Ramsdell, "Studies on silicon carbide," *Am. Mineral.*, vol. 32, no. 1–2, pp. 64–82, 1947.

[59] J. D. H. Donnay, G. Donnay, A. C. Association, and others, *Crystal data: determinative tables*, vol. 547. American Crystallographic Association Buffalo, NY, 1963.

[60] A. Taylor, R. M. Jones, H. R. Philipp, and E. A. Taft, "Silicon Carbide—A High Temperature Semiconductor," in *Proc. Conf. on Silicon Carbide (Boston, MA 1959)*, 1960, pp. 147–154.

[61] G. A. Slack, "Thermal conductivity of pure and impure silicon, silicon carbide, and diamond," *J. Appl. Phys.*, vol. 35, no. 12, pp. 3460–3466, 1964.

[62] K. H. Hellwege and O. Madelung, "Numerical Data and Functional Relationships in Science and Technology, vol. 17a and 22a." Springer-Verlag New York, 1982.

[63] G. L. Harris, *Properties of silicon carbide*, no. 13. Iet, 1995.

[64] P. G. Neudeck, "Progress in silicon carbide semiconductor electronics technology," *J. Electron. Mater.*, vol. 24, no. 4, pp. 283–288, 1995.

[65] T. Seyller, A. Bostwick, K. V Emtsev, K. Horn, L. Ley, J. L. McChesney, T. Ohta, J. D. Riley, E. Rotenberg, and F. Speck, “Epitaxial graphene: a new material,” *Phys. status solidi*, vol. 245, no. 7, pp. 1436–1446, 2008.

[66] C. Çelebi, C. Yan\ik, A. G. Demirkol, and \.Ismet \.I Kaya, “The effect of a SIC cap on the growth of epitaxial graphene on SIC in ultra high vacuum,” *Carbon N. Y.*, vol. 50, no. 8, pp. 3026–3031, 2012.

[67] D. G. Senesky, B. Jamshidi, K. B. Cheng, and A. P. Pisano, “Harsh environment silicon carbide sensors for health and performance monitoring of aerospace systems: A review,” *Sensors Journal, IEEE*, vol. 9, no. 11, pp. 1472–1478, 2009.

[68] S. Shivaraman, L. H. Herman, F. Rana, J. Park, and M. G. Spencer, “Schottky barrier inhomogeneities at the interface of few layer epitaxial graphene and silicon carbide,” *Appl. Phys. Lett.*, vol. 100, no. 18, p. 183112, 2012.

[69] O. Kazakova, V. Panchal, and T. L. Burnett, “Epitaxial graphene and graphene--based devices studied by electrical scanning probe microscopy,” *Crystals*, vol. 3, no. 1, pp. 191–233, 2013.

[70] W. A. De Heer, C. Berger, M. Ruan, M. Sprinkle, X. Li, Y. Hu, B. Zhang, J. Hankinson, and E. Conrad, “Large area and structured epitaxial graphene produced by confinement controlled sublimation of silicon carbide,” *Proc. Natl. Acad. Sci.*, vol. 108, no. 41, pp. 16900–16905, 2011.

[71] S. Shivaraman, M. V. S. Chandrashekhar, J. J. Boeckl, and M. G. Spencer, “Thickness estimation of epitaxial graphene on SiC using attenuation of substrate raman intensity,” *J. Electron. Mater.*, vol. 38, no. 6, pp. 725–730, 2009.

[72] W.-C. Lien, D.-S. Tsai, D.-H. Lien, D. G. Senesky, H. He, and A. P. Pisano, “4H--SiC Metal--Semiconductor--Metal Ultraviolet Photodetectors in Operation of 450,” *Electron Device Lett. IEEE*, vol. 33, no. 11, pp. 1586–1588, 2012.

[73] C. O. Chui, A. K. Okyay, and K. C. Saraswat, “Effective dark current suppression with asymmetric MSM photodetectors in group IV semiconductors,” *Photonics Technol. Lett. IEEE*, vol. 15, no. 11, pp. 1585–1587, 2003.

[74] T. Mueller, F. Xia, and P. Avouris, “Graphene photodetectors for high-speed optical communications,” *Nat. Photonics*, vol. 4, no. 5, pp. 297–301, 2010.

[75] Y. Q. An, J. E. Rowe, D. B. Dougherty, J. U. Lee, and A. C. Diebold, “Optical second-harmonic generation induced by electric current in graphene on Si and SiC substrates,” *Phys. Rev. B*, vol. 89, no. 11, p. 115310, 2014.

[76] Y. Lu, M. B. Lerner, Z. J. Qi, J. J. Mitala Jr, J. H. Lim, B. M. Discher, and A. T. C. Johnson, “Graphene-protein bioelectronic devices with wavelength-dependent photoresponse,” *Appl. Phys. Lett.*, vol. 100, no. 3, p. 33110, 2012.

[77] G. Konstantatos, M. Badioli, L. Gaudreau, J. Osmond, M. Bernechea, F. P. G. de Arquer, F. Gatti, and F. H. L. Koppens, “Hybrid graphene-quantum dot phototransistors with ultrahigh gain,” *Nat. Nanotechnol.*, vol. 7, no. 6, pp. 363–368, 2012.

[78] C.-M. Chou, H.-T. Cho, V. K. S. Hsiao, K.-T. Yong, and W.-C. Law, “Quantum dot-doped porous silicon metal--semiconductor metal photodetector,” *Nanoscale Res. Lett.*, vol. 7, no. 1, pp. 1–4, 2012.

[79] Y. Zhu, Z. Li, M. Chen, H. M. Cooper, G. Q. M. Lu, and Z. P. Xu, “One-pot preparation of highly fluorescent cadmium telluride/cadmium sulfide quantum dots under neutral-pH condition for biological applications,” *J. Colloid Interface Sci.*, vol. 390, no. 1, pp. 3–10, 2013.

[80] J. Tang and E. H. Sargent, “Infrared colloidal quantum dots for photovoltaics: fundamentals and recent progress,” *Adv. Mater.*, vol. 23, no. 1, pp. 12–29, 2011.

[81] T. Kawawaki and T. Tatsuma, “Enhancement of PbS quantum dot-sensitized photocurrents using plasmonic gold nanoparticles,” *Phys. Chem. Chem. Phys.*, vol. 15, no. 46, pp. 20247–20251, 2013.